Chinese Journal of Natural Medicines

Icariin enhances PINK1–associated mitophagy to attenuate NLRP3/GSDMD–related microglial pyroptosis and cognitive impairment in Alzheimer’s disease

Longmin Fan, Haitao Jiang, Min Yi, Weijun Peng, Zheyu Zhang

Citation: Longmin Fan, Haitao Jiang, Min Yi, Weijun Peng, Zheyu Zhang, Icariin enhances PINK1–associated mitophagy to attenuate NLRP3/GSDMD–related microglial pyroptosis and cognitive impairment in Alzheimer’s disease, Chinese Journal of Natural Medicines, 2026, 24(10), 1176–1190. doi: 10.1016/S1875–5364(26)61213–7.

View online: https://doi.org/10.1016/S1875–5364(26)61213–7

Related articles that may interest you

Reynosin protects neuronal cells from microglial neuroinflammation by suppressing NLRP3 inflammasome activation mediated by NADPH oxidase

Chinese Journal of Natural Medicines. 2024, 22(6), 486–500 https://doi.org/10.1016/S1875–5364(24)60652–7

10,11–Dehydrocurvularin attenuates inflammation by suppressing NLRP3 inflammasome activation

Chinese Journal of Natural Medicines. 2023, 21(3), 163–171 https://doi.org/10.1016/S1875–5364(23)60418–2

Mangiferin inhibited neuroinflammation through regulating microglial polarization and suppressing NF–κB, NLRP3 pathway

Chinese Journal of Natural Medicines. 2021, 19(2), 112–119 https://doi.org/10.1016/S1875–5364(21)60012–2

Hernandezine promotes cancer cell apoptosis and disrupts the lysosomal acidic environment and cathepsin D maturation

Chinese Journal of Natural Medicines. 2024, 22(5), 387–401 https://doi.org/10.1016/S1875–5364(24)60638–2

An inulin–type fructan CP–A from *Codonopsis pilosula* attenuates experimental colitis in mice by promoting autophagy–mediated inactivation of NLRP3 inflammasome

Chinese Journal of Natural Medicines. 2024, 22(3), 249–264 https://doi.org/10.1016/S1875–5364(24)60556–X

Approved drugs and natural products at clinical stages for treating Alzheimer’s disease

Chinese Journal of Natural Medicines. 2024, 22(8), 699–710 https://doi.org/10.1016/S1875–5364(24)60606–0

Wechat

Chinese Journal of Natural Medicines 24 (2026) 1176-1190

Contents lists available at ScienceDirect

Chinese Journal of Natural Medicines

journal homepage: www.cjnmcpu.com/



Original article

Icariin enhances PINK1-associated mitophagy to attenuate NLRP3/GSDMD-related microglial pyroptosis and cognitive impairment in Alzheimer's disease

Longmin Fan, Haitao Jiang, Min Yi, Weijun Peng*, Zheyu Zhang*

Department of Integrated Traditional Chinese & Western Medicine, The Second Xiangya Hospital, Central South University, Changsha 410011, China

ARTICLE INFO

Article history:
Received 4 January 2026
Revised 20 July 2026
Accepted 24 July 2026
Available online 20 October 2026

Keywords:
Alzheimer's disease
Icariin
mitophagy
NLRP3 inflammasome
Microglial pyroptosis

ABSTRACT

Alzheimer's disease (AD) is a progressive neurodegenerative disorder in which microglia-mediated neuroinflammation contributes to disease progression. Icariin (ICA), a major bioactive flavonoid from *Epimedium*, has neuroprotective activity, but how it regulates mitochondrial quality control and inflammatory injury in microglia remains unclear. In the present study, APP/PS1 transgenic mice and $A\beta_{1-42}$-stimulated BV-2 microglia were used to examine the effects of ICA on mitophagy, mitochondrial stress, NLRP3/GSDMD-related pyroptotic changes, and neuroinflammation. Behavioral testing, histological analysis, transcriptomic profiling, immunofluorescence, Western blotting, ELISA, molecular docking, molecular dynamics simulation, cellular thermal shift assay, Mdivi-1 co-treatment, and siRNA-mediated *Pink1* knockdown were performed. ICA improved cognitive deficits in APP/PS1 mice and reduced microglial inflammatory activation. Transcriptomic and experimental analyses showed that ICA enhanced mitophagy-related responses, restored mitochondrial membrane potential, and reduced excessive mitochondrial reactive oxygen species accumulation. Molecular docking, molecular dynamics simulation, and cellular thermal shift assay supported potential engagement of ICA with PINK1. ICA also reduced NLRP3 inflammasome-associated inflammatory injury, GSDMD-related pyroptotic changes, and IL-1β and IL-18 release. In APP/PS1 mice, Mdivi-1 co-treatment weakened the anti-inflammatory effects of ICA. In $A\beta_{1-42}$-stimulated BV-2 microglia, *Pink1* knockdown reduced ICA-induced LC3/TOM20 colocalization and partially reversed the inhibitory effects of ICA on NLRP3 inflammasome-associated inflammatory markers. Overall, ICA enhances PINK1-associated mitophagy, alleviates mitochondrial stress, and attenuates NLRP3/GSDMD-related microglial pyroptotic injury in AD-related models. These findings suggest that PINK1-associated mitochondrial quality control contributes to the neuroprotective effects of ICA.

1. Introduction

Alzheimer's disease (AD) is a prevalent neurodegenerative disorder, characterized primarily by progressive cognitive decline [1]. More than 55 million individuals worldwide are currently affected, and this number is projected to rise to 139 million by 2050, posing an enormous burden on global public health systems [2, 3]. Although therapeutic strategies targeting β-amyloid (Aβ), tau pathology, and neuroinflammation have been extensively investigated, current treatments provide primarily symptomatic relief or modestly slow disease progression, with a limited ability to halt or reverse the underlying pathology [4]. Therefore, identifying novel therapeutic targets and developing more effective interventions remain urgent clinical and scientific priorities.

Microglia are the principal innate immune effector cells of the central nervous system (CNS) and are essential for maintaining tissue homeostasis, pruning synapses, and clearing metabolic waste under physiological conditions [5, 6]. However, upon exposure to damage-associated molecular patterns (DAMPs) or aberrant pathological proteins, microglia rapidly shift from a surveillant to an activated state, producing large amounts of inflammatory mediators and initiating neuroinflammatory responses that ultimately contribute to neuronal injury [7]. Extensive evidence indicates that excessive or sustained microglial activation is a major driver of AD onset and progression, and the degree of microglial activation is closely associated with cognitive decline [8, 9]. Therefore, strategies aimed at modulating microglial functional states represent a critical therapeutic opportunity to attenuate neuroinflammation and slow AD pathogenesis.

Among various pro-inflammatory signaling pathways, the NLR family pyrin domain-containing 3 (NLRP3) inflammasome is a key cytosolic multiprotein complex highly expressed in microglia, playing a central role in AD-associated neuroinflammation [10, 11]. Upon sensing danger signals such as Aβ aggregates, tau fibrils, or DAMPs, NLRP3 undergoes conformational changes and recruits the adaptor protein apoptosis-associated speck-like protein containing a CARD (ASC) through homotypic domain interactions [12]. ASC then recruits pro-caspase-1 through CARD-CARD interactions, promoting NLRP3 inflammasome assembly and caspase-1 autocleavage. Activated caspase-1 triggers downstream

* Corresponding author.
E-mail addresses: pengweijun87@csu.edu.cn (W. Peng); zhangzy3904@csu.edu.cn (Z. Zhang)

https://doi.org/10.1016/S1875-5364(26)61213-7
Copyright © 2026, China Pharmaceutical University. Published by Elsevier B.V. All rights are reserved.

inflammatory responses through two principal mechanisms [13]. First, it cleaves gasdermin D (GSDMD) to generate the membrane-permeabilizing GSDMD N-terminal fragment, which translocates to the plasma membrane, oligomerizes to form transmembrane pores, disrupts membrane integrity, and induces pyroptosis of microglia. Second, caspase-1 processes pro-IL-1β and pro-IL-18 into their mature bioactive forms, which are subsequently released through GSDMD pores, thereby amplifying neuroinflammation and promoting neuronal degeneration [14]. Given its pivotal role in driving inflammatory cell death and neuroimmune dysregulation, the NLRP3/GSDMD-mediated pyroptosis pathway has emerged as a promising therapeutic target for limiting microglial overactivation and attenuating AD-related neuroinflammation.

Growing evidence indicates that mitochondrial dysfunction is a major upstream driver of abnormal NLRP3 inflammasome activation [15]. Damaged mitochondria generate excessive reactive oxygen species (ROS) and release pro-inflammatory signals such as mitochondrial DNA (mtDNA), both of which can directly promote NLRP3 assembly and activation, triggering microglial pyroptosis and amplifying neuroinflammation [16, 17]. Studies have demonstrated that impaired mitophagy markedly enhances NLRP3-mediated neuroinflammation, whereas restoring or promoting mitophagy effectively suppresses inflammasome activation, attenuates microglial pyroptosis, and improves cognitive deficits in aging-related disorders [13, 18]. However, the number of pharmacological agents that specifically target mitophagy in AD remains limited. Thus, therapeutic strategies that modulate mitophagy hold considerable promise for mitigating neuroinflammation and slowing AD progression.

Icariin (ICA), a major flavonoid compound extracted from the traditional medicinal herb *Epimedium*, has been well documented for its anti-inflammatory, antioxidant, and neuroprotective properties [19, 20]. Previous studies indicate that ICA can suppress neuroinflammatory responses *via* multiple signaling pathways, including AKT1, NF-κB, tumor necrosis factor (TNF), and PRKCA, and can ameliorate learning and memory deficits across various neurological disease models [21-23]. Furthermore, recent findings show that ICA improves mitochondrial function and enhances mitophagy in models of depression [24], suggesting that it may have broader regulatory potential in maintaining mitochondrial homeostasis. However, it remains unknown whether ICA can enhance mitophagy in the context of AD, thereby reducing mitochondria-derived inflammatory signals and suppressing NLRP3 inflammasome activation and its downstream GSDMD-mediated pyroptosis. To date, no direct evidence has demonstrated whether ICA can modulate excessive microglial activation in AD through this mechanism, and the underlying regulatory pathways remain unclear.

In this study, we employed both APP/PS1 transgenic mice and Aβ-stimulated BV-2 microglial cells to investigate the role of mitophagy in regulating NLRP3 inflammasome activation and pyroptosis in AD. We further evaluated whether ICA attenuates NLRP3/GSDMD-dependent microglial pyroptosis by promoting mitophagy and ultimately improves AD-related cognitive impairment.

2. Materials and methods

2.1. Reagents

Icariin (ICA, ≥ 98%, MCE, HY-N0014) and donepezil hydrochloride (≥ 98%, MCE, HY-B0034) were purchased from MedChemExpress (Shanghai, China). Mdivi-1 (Selleck Chemicals, S7162) was obtained from Selleck Chemicals (Houston, TX). Primary antibodies used in this study included anti-IBA1 (AWA11292, 1∶200, Abiowell, China), anti-CD68 (#97778, 1∶400, Cell Signaling Technology, Danvers, MA, USA), anti-NLRP3 (ab270449, 1∶50; ab263899, 1∶1000, Abcam, Cambridge, UK), anti-PINK1 (A7131, 1∶2500, ABclonal), anti-caspase-1 (ab207802, 1∶1000, Abcam), anti-IL-18 (A24169PM, 1∶2000, ABclonal), anti-IL-1β (A27676, 1∶3000, ABclonal), anti-LC3 (T55992, 1∶100, Abmart, Shanghai, China), anti-TOM20 (T55527, 1∶1000, Abmart), and anti-GAPDH (EM1101, 1∶10 000, Huabio). HRP-conjugated goat anti-rabbit IgG (RGAR004, 1∶200, Proteintech) and HRP-conjugated goat anti-mouse IgG (RGAM002, 1∶500, Proteintech) were used as secondary antibodies for Western blotting. Alexa Fluor 488/594-conjugated goat anti-rabbit IgG and goat anti-mouse IgG secondary antibodies were used for immunofluorescence staining. Unless otherwise stated, all chemicals and reagents used in this study were of analytical grade.

2.2. Preparation of $A\beta_{1-42}$ oligomers

$A\beta_{1-42}$ peptide (≥ 95% purity; Millipore Sigma) was first dissolved in hexafluoroisopropanol (HFIP, Chemicalbook, Beijing, China) and incubated at room temperature for 1 h to remove pre-aggregated species. The solution was evaporated using a SpeedVac concentrator to obtain a dry peptide film, which was stored at −80 °C until use [25]. For experiments, the peptide film was dissolved in anhydrous DMSO to 5 mmol·L^{-1}, vortexed briefly, and diluted to 100 μmol·L^{-1} in serum-free, phenol red-free medium. The solution was incubated at 4 °C for 24 h to form oligomers, then centrifuged at 14 000 × *g* for 10 min. The supernatant containing soluble $A\beta_{1-42}$ oligomers was collected for subsequent experiments.

2.3. Cell culture and treatment

BV-2 murine microglial cells were cultured in Dulbecco's Modified Eagle Medium supplemented with 10% fetal bovine serum at 37 °C in a 5% CO_2 atmosphere. Based on preliminary dose-response experiments, 40 μmol·L^{-1} ICA was selected for subsequent *in vitro* studies because it exerted a significant protective effect without evident cytotoxicity. Cells were pretreated with ICA (40 μmol·L^{-1}) for 24 h, followed by exposure to $A\beta_{1-42}$ (10 μmol·L^{-1}) for an additional 24 h to establish an *in vitro* Aβ-induced injury model.

2.4. Cell death assays

Cell death was evaluated using a lactate dehydrogenase (LDH) release assay (Solarbio, Beijing, China) and propidium iodide (PI) staining (Beyotime, Shanghai, China). The LDH levels in the culture media were measured according to the manufacturer's protocol. For PI staining, cells were incubated with PI (4 μg·mL^{-1}) and Calcein-AM (4 μg·mL^{-1}) for 10 min. Images were acquired using an INCell Analyzer 2500 system (GE Healthcare, Pittsburgh, PA).

2.5. ROS measurement

Intracellular ROS levels were determined using an ROS Detection Kit (Solarbio, Beijing, China). Cells were incubated with DCFH-DA at 37 °C for 20 min, washed, and analyzed by flow cytometry.

2.6. Ethics statement

All animal procedures were approved by the Animal Ethics Committee of the Second Xiangya Hospital, Central South University, China (Approval No. 2021226) and performed in accordance with the National Institutes of Health Guide for the Care and

Use of Laboratory Animals.

2.7. Animals and drug treatment

Six-month-old male C57BL/6J wild-type and APP/PS1 transgenic mice (25–30 g; Cyagen Biosciences, Guangzhou, China) were used to avoid potential confounding effects of the estrous cycle on cognition. Animals were maintained under standard conditions (22 ± 2 °C, 50% ± 10% humidity, 12-h light/dark cycle) with ad libitum access to food and water. Mice were randomly allocated to six groups (n = 8–10 per group): (1) WT Control: C57BL/6J mice receiving vehicle (saline, p.o.). (2) APP/PS1 Model: APP/PS1 mice receiving vehicle (saline, p.o.). (3) APP/PS1 + Donepezil: APP/PS1 mice receiving donepezil hydrochloride (3 mg·kg^{-1}, p.o.) as a positive control to validate the model and benchmark therapeutic efficacy. (4) APP/PS1 + ICA: APP/PS1 mice receiving ICA (100 mg·kg^{-1}, p.o.) [26]. (5) APP/PS1 + Mdivi-1: APP/PS1 mice receiving Mdivi-1 (25 mg·kg^{-1}, i.p.) to evaluate mitophagy-related mechanisms. (6) APP/PS1 + ICA + Mdivi-1: APP/PS1 mice receiving ICA (100 mg·kg^{-1}, p.o.) plus Mdivi-1 (25 mg·kg^{-1}, i.p.) to evaluate mitophagy-related mechanisms. All treatments were administered daily for 100 consecutive days.

2.8. Behavioral test

Behavioral tests were performed sequentially between 08:30 and 12:30 in a sound-attenuated room with dim lighting. The mice were acclimatized for 30 min before testing. The observers were blinded to group allocation.

2.8.1. Nest-building test

Mice were kept alone in a cage for 24 h to allow them to adapt to the environment. Then, a 5 cm × 5 cm piece of cotton fiber nesting material was placed in each mouse's cage [27]. Nests were scored at 2 and 12 h after the start of the test according to the criteria listed in Table S1.

2.8.2. Novel object recognition (NOR) test

The NOR test was conducted according to established protocols [28]. For the first 3 days before testing, mice were habituated to handling for 5 min daily. During the familiarization phase, two identical objects were placed in the adjacent corners of a 50 cm × 50 cm × 50 cm square arena, and the mice were allowed to explore for 5 min. After a 24-h memory interval, one object was replaced with a novel object, and the mice were allowed to explore freely for an additional 5 min. Exploration was defined as sniffing or touching objects within a 3 cm radius.

2.8.3. Open field test (OFT)

Motor activities and anxiety-like behaviors were evaluated in a 45 cm × 45 cm × 45 cm white opaque arena [29]. Each mouse was placed in the corner of the arena facing the wall and allowed to explore freely for 5 min. Total distance walked and time spent in the central area were automatically recorded.

2.8.4. Y-maze test

Spontaneous alternation behavior was assessed using a Y-maze apparatus (21 cm × 7 cm × 15.5 cm arms at 120° angles; Shanghai Xinruan, China) [30]. During the training phase, one arm was blocked, and the mice were allowed to explore the two open arms for 10 min. After a 1-h interval, the mice were returned into the maze with all arms accessible and allowed to explore freely for 5 min. The percentage of spontaneous alternations was calculated to assess working memory.

2.8.5. Elevated plus maze (EPM)

The EPM consisted of two open arms (50 cm × 10 cm × 0.5 cm) and two closed arms (50 cm × 10 cm × 20 cm) elevated 50 cm above the floor. Each mouse was placed on a central platform (10 cm × 10 cm) facing an open arm and allowed to explore freely for 5 min. The time spent in the open and closed arms, and the total distance traveled, were recorded to assess anxiety-like behavior [31].

2.8.6. Morris water maze (MWM) test

The MWM test was performed in a circular pool (120 cm in diameter, 45 cm in height) filled with opaque water and maintained at 22 ± 1 °C [32]. During the training phase, mice were placed in water in different quadrants and trained to find the hidden platform 1 cm below the water surface. Each mouse was tested three times a day. If a mouse failed to find the platform within 60 s, it was guided to the platform and allowed to remain there for 30 s. On day 7, the platform was removed and a probe trial was conducted to evaluate spatial memory. An automated video-tracking system was used to record escape latency, the number of platform crossings, time spent in the target quadrant, and swimming speed.

2.9. Transmission electron microscopy (TEM)

After washing three times with PBS, the tissues were fixed in 0.1 mol·L^{-1} PBS with 1% osmium tetroxide for 1 h, dehydrated by graded acetone (30%, 50%, 70%, 90%, and 100%, each for 10 min), and impregnated successively with propylene oxide/Epon 812 (1∶1, 1 h) and pure Epon 812 (2 h, 37 °C). The samples were polymerized at 60 °C for 48 h. Ultrathin sections (70 nm) were cut on the Leica EM UC7 ultramicrotome, stained with uranyl acetate and lead citrate (5 min each), and detected at 80 kV using a FEI Tecnai G2 transmission electron microscope. Images were obtained from five non-overlapping regions of each animal for mitochondrial morphology and autophagosome quantification.

2.10. Western blotting

Hippocampal tissue and BV-2 microglial cells were lysed in ice-cold radioimmunoprecipitation assay buffer (Epizyme Biotech, Shanghai, China) with protease and phosphatase inhibitors (Epizyme Biotech). The lysates were incubated on ice for 30 min, rotated intermittently every 10 min, and then centrifuged at 12 000 × g for 10 min at 4 °C to remove debris. Proteins were separated by SDS-PAGE and transferred onto PVDF membranes. Membranes were blocked with 5% milk in Tris-buffered saline containing Tween-20 for 2 h at room temperature and then incubated with primary antibodies diluted in 3% bovine serum albumin overnight at 4 °C. The protein bands were visualized by chemiluminescence (ECL; NCM Biotech, Jiangsu, China) and imaged using an Odyssey imaging system (LI-COR Biosciences, Lincoln, NE).

2.11. Immunofluorescence (IF)

After transcardial perfusion with 4% paraformaldehyde under anesthesia, the brain tissues were post-fixed overnight at 4 °C and sequentially cryopreserved in 20% and 30% sucrose solutions. The tissues were embedded in an optimal cutting temperature compound and frozen vertically at 15-μm thickness using a cryostat (RWD Life Science, Shenzhen, China). Sections were air-dried for 15 min at room temperature, rinsed with PBS, permeabilized with 0.3% Triton X-100 for 15 min, and blocked with 5% BSA for 1 h. Sections were incubated with primary antibodies overnight at 4 °C. After washing, sections were incubated with fluorescent secondary antibodies for 1 h at 37 °C. Nuclei were counterstained with mounting medium (Solarbio, Beijing, China) containing DAPI. Images were acquired using a Zeiss LSM800 confocal microscope (Carl Zeiss, Oberkochen, Germany).

2.12. Reverse transcription and real-time quantitative polymerase chain reaction (RT-qPCR)

Total ribonucleic acid (RNA) was extracted from the hippocampal tissues and BV-2 microglial cells using a column purification kit (Accurate Biology, Hunan, China) following the manufacturer's protocol. cDNA was synthesized using a reverse transcription kit. qPCR was conducted using SYBR Green chemistry, and relative gene expression levels were calculated by the $2^{-\Delta\Delta CT}$ method. The primers used are shown in Table S2.

2.13. RNA sequencing (RNA-seq) and bioinformatics analysis

RNA-seq libraries were prepared from high-quality RNA samples. Sequence quality was assessed using FastQC (v0.11.5), and low-quality reads were filtered using NGSQC (v2.3.3). Gene expression was quantitatively analyzed using StringTie (v1.3.3b). Differentially expressed genes (DEGs) were identified using DESeq (v1.28.0), with $|\log_2$ fold change$| \geq 1$ and $P \leq 0.05$. Visualization (volcano plots and heat maps) was performed using R software (v4.0.3).

2.14. Molecular docking

The two-dimensional structure of ICA was obtained from the PubChem database and imported into Chem3D 23.1.1 to generate and optimize the three-dimensional structure. The optimized ligand structure was saved in mol2 format. The high-resolution crystal structure of PINK1 was obtained from the RCSB Protein Data Bank. Water molecules, phosphate groups, and other non-essential heteroatoms were removed using PyMOL 2.6, and the processed protein structure was saved in PDB format. The protein and ligand structures were prepared using AutoDockTools, including hydrogen addition, charge assignment, and definition of rotatable bonds for the ligand. Molecular docking was performed using AutoDock Vina 1.2.5. The docking grid box was defined around the active pocket of PINK1. The optimal docking pose was selected according to the docking affinity score and the plausibility of the ligand-binding conformation. Protein–ligand interactions were visualized and analyzed using Discovery Studio Visualizer.

2.15. Molecular dynamics simulation and MM/PBSA binding free-energy analysis

The predicted ICA-PINK1 complex obtained from molecular docking was used as the initial structure for molecular dynamics simulation in GROMACS 2022.2. Force-field parameters for PINK1 were generated with the AMBER14SB force field. The ligand topology of ICA was generated using sobtop_1.0 (dev3.1) with the GAFF2 force field, and ligand charges were assigned by the RESP method. The complex was solvated in a TIP3P water box, with a minimum distance of 1.0 nm between the protein and the box edge. Na^+ and Cl^- ions were added using the gmx genion tool to neutralize the system and establish a final NaCl concentration of 0.15 mol·L^{-1}.

Long-range electrostatic interactions were calculated using the particle mesh Ewald method, with a cutoff distance of 1.0 nm. Covalent bonds were constrained using the LINCS algorithm. Before the production run, the system was energy-minimized by 3000 steps of steepest descent minimization followed by 2000 steps of conjugate-gradient minimization. A 100-ns production simulation was then performed in the NPT ensemble with a 2-fs integration time step. The temperature was maintained at 310 K using the Nosé–Hoover thermostat with a coupling constant of 0.1 ps, and the pressure was maintained at 1 bar using the Parrinello–Rahman barostat with a coupling constant of 2.0 ps.

Trajectory analyses were conducted using GROMACS 2022.2. Root-mean-square deviation, root-mean-square fluctuation, hydrogen-bond number, radius of gyration, solvent-accessible surface area, and Gibbs free-energy landscape were calculated using gmx rmsd, gmx rmsf, gmx hbond, gmx gyrate, gmx sasa, and gmx sham, respectively. MM/PBSA binding free energy was calculated using the gmx_MMPBSA package.

2.16. Cellular thermal shift assay

The cellular thermal shift assay was performed as previously described with minor modifications. BV-2 cells were incubated in FBS-free medium containing vehicle or ICA at 40 μmol·L^{-1} for 2 h. Cells were collected, washed with cold PBS, resuspended in PBS, and lysed by three freeze-thaw cycles. Lysates from the vehicle- and ICA-treated groups were divided into equal aliquots and heated at 37, 43, 46, 49, 52, and 55 °C for 3 min. Samples were then kept at 4 °C for 15 min and centrifuged at 12 000 r·min^{-1} for 15 min at 4 °C. The supernatants containing soluble proteins were collected and analyzed by Western blotting with an anti-PINK1 antibody. Band intensities were quantified and normalized to the corresponding 37 °C sample within each group.

2.17. siRNA-mediated Pink1 knockdown

Small interfering RNAs targeting mouse *Pink1* were purchased from GeneChem Co., Ltd. (Shanghai, China). The sequences were as follows: si-PINK1-1 sense, 5′-CCCUUUGCCAUCAAGAUGAdTdT-3′ and antisense, 5′-UCAUCUUGAUGGCAAAGGGdTdT-3′; si-PINK1-2 sense, 5′-GGAUUAUCUGAUAGGGCAAdTdT-3′ and antisense, 5′-UUGCCCUAUCAGAUAAUCCdTdT-3′. BV-2 cells were seeded in six-well plates at a density of 2×10^5 cells per well 24 h before transfection. When the cell confluence reached approximately 50%–70%, cells were transfected with negative-control siRNA (siNC) or *Pink1*-targeting siRNAs using Lipo6000™ transfection reagent according to the manufacturer's instructions. After transfection for 24 h, the knockdown efficiency of *PINK1* was evaluated by Western blotting and RT-qPCR. Because si-PINK1-2 showed stronger knockdown efficiency at both the protein and mRNA levels, si-PINK1-2 was selected for subsequent experiments.

2.18. Statistical analysis

Statistical analyses were performed using GraphPad Prism v 8.0.2 (GraphPad Software, San Diego, CA, USA). Normality was assessed using the Shapiro-Wilk test, and homogeneity of variance was evaluated using Levene's test. For comparisons among multiple groups with a single factor, one-way ANOVA followed by Bonferroni's post hoc test was used when assumptions of normality and homogeneity of variance were satisfied. When normality was satisfied but homogeneity of variance was violated, Welch's ANOVA followed by Games-Howell post hoc test was applied. When normality was not satisfied, the Kruskal-Wallis test followed by Dunn's multiple comparisons test was used. For comparisons involving two independent variables, two-way ANOVA followed by Bonferroni's multiple-comparisons test was used. For comparisons between two groups, an unpaired two-tailed Student's *t*-test was used when assumptions were satisfied; otherwise, the Mann-Whitney *U* test was applied. Data are presented as mean ± SD. All tests were two-sided, and $P < 0.05$ was considered statistically significant.

3. Results

3.1. ICA improves cognitive impairment in APP/PS1 mice

To evaluate the effect of ICA on AD-related cognitive deficits,

multiple behavioral tests were performed (Fig. 1A). In the nest-building test, APP/PS1 mice showed markedly lower nesting scores than controls ($P < 0.05$), whereas ICA treatment significantly increased these scores ($P < 0.01$) to a level comparable to donepezil (Fig. 1B). In the NOR test, APP/PS1 mice displayed a significantly reduced discrimination index ($P < 0.001$), which improved markedly following ICA treatment ($P < 0.01$) (Fig. 1C). In the OFT and EPM, APP/PS1 mice showed pronounced anxiety-like behaviors. ICA significantly increased the time spent in the central area and in the open arms ($P < 0.05$), suggesting that ICA alleviated anxiety-like behavior (Figs. 1D and 1E). In the Y-maze test, APP/PS1 mice exhibited reduced exploration of the novel arm ($P < 0.001$), whereas both ICA and donepezil treatments significantly improved this deficit ($P < 0.001$) (Fig. 1F).

During the MWM training phase, APP/PS1 mice showed prolonged escape latency and traveled a significantly longer path to reach the hidden platform than controls ($P < 0.05$). Both ICA and donepezil treatments shortened escape latency and reduced path length, with learning curves approaching those of the control group. In the probe trial, APP/PS1 mice exhibited significantly reduced swimming distance in the target quadrant ($P < 0.001$), shorter dwell time in the platform-surrounding corridor ($P < 0.01$), and fewer platform crossings ($P < 0.01$). ICA significantly improved these memory-related parameters ($P < 0.05$). Swimming speed was analyzed to assess potential locomotor differences. APP/PS1 mice displayed significantly reduced swimming speed compared with controls, whereas ICA or donepezil treatments significantly increased swimming speed relative to untreated APP/PS1 mice (Fig. 1G).

3.2. ICA inhibits excessive activation of microglia

Microglia are the primary immune cells of the CNS and rapidly shift from a quiescent to an activated state under pathological conditions [33]. To assess microglial activation in APP/PS1 mice, we examined microglia in the hippocampal CA1, CA3, and DG regions using IBA1/CD68 dual IF staining (Fig. 2A). Quantitative analyses showed that APP/PS1 mice had a significantly higher density of $IBA1^+$ microglia ($P < 0.05$) and a markedly increased proportion of $CD68^+IBA1^+$ double-positive cells ($P < 0.001$) compared with controls. Both ICA and donepezil treatments significantly reduced microglial density ($P < 0.05$) and the proportion of double-positive cells ($P < 0.001$) (Figs. 2B and 2C).

To further evaluate overall activation, the $IBA1^+$ area fraction in the hippocampus was significantly increased in APP/PS1 mice ($P < 0.001$) and was markedly reduced following ICA treatment ($P < 0.01$) (Fig. 2D). ELISA results showed elevated levels of IL-6 and TNF-α in APP/PS1 mice ($P < 0.001$), whereas ICA significantly decreased both cytokines ($P < 0.01$) (Figs. 2E and 2F).

3.3. ICA enhances mitophagy in hippocampus and alleviates mitochondrial stress

To further investigate the mechanisms underlying the protective effects of ICA, we performed RNA-seq analysis on hippocampal tissue from APP/PS1 mice. The results showed that several mitophagy-related genes, including *Pink1*, *Atg4b*, and *Fosl2*, were upregulated after ICA treatment compared with the APP/PS1 group (Fig. 3A). KEGG enrichment analysis of differentially expressed genes further revealed significant enrichment of the mitophagy pathway (mmu04137) (Fig. 3B). Consistent with the transcriptomic findings, RT-qPCR analysis confirmed that ICA significantly increased the expression of *Pink1*, *Lc3b*, *Atg4b*, and *Becn1* in the hippocampus (Fig. S1A), supporting the involvement of mitophagy-related processes.

To further assess ultrastructural alterations, hippocampal tissue was examined by TEM. In the AD group, hippocampal cells exhibited swollen mitochondria, disrupted cristae, and increased structural damage. These pathological changes were alleviated after ICA treatment, accompanied by increased autophagosome-like structures (Fig. 3C). To determine whether ICA enhanced mitophagy in microglia, we performed IF co-staining of IBA1, LC3, and TOM20. Compared with the AD group, the ICA treatment group showed increased LC3 fluorescence intensity, enhanced LC3/TOM20 colocalization, and increased LC3/TOM20 colocalization within IBA1-positive microglia (Fig. 3D and Fig. S1B), providing more direct evidence that ICA promoted mitophagy in hippocampal microglia.

To further examine the relationship between ICA-mediated mitophagy and mitochondrial stress, an $A\beta_{1-42}$-induced BV-2 microglial injury model was established *in vitro*. CCK-8 assays showed that 10 μmol·L^{-1} $A\beta_{1-42}$ significantly reduced cell viability, whereas ICA treatment partially restored cell survival (Figs. S1C and S1D). Based on the dose-response results, 40 μmol·L^{-1} ICA was selected for the subsequent *in vitro* experiments (Fig. S1E). JC-1 staining showed that $A\beta_{1-42}$ markedly decreased mitochondrial membrane potential, whereas ICA significantly increased the red/green fluorescence ratio and partially restored mitochondrial membrane potential (Figs. 3E and 3F). Flow cytometry and ROS fluorescence staining further demonstrated that ICA markedly reduced $A\beta_{1-42}$-induced intracellular ROS accumulation (Figs. 3G and 3H, Figs. S1F and S1G). In addition, LC3 and MitoTracker co-staining showed that ICA treatment increased LC3 puncta formation and enhanced LC3-mitochondria colocalization compared with the $A\beta_{1-42}$-treated group (Fig. 3I, Figs. S1H and S1I). Western blotting further showed that ICA restored PINK1 protein expression in $A\beta_{1-42}$-stimulated BV-2 microglia (Figs. 3J and 3K), consistent with the transcriptomic and RT-qPCR findings. Together, these results suggest that ICA enhances PINK1-associated mitophagy-related mitochondrial quality control and alleviates mitochondrial stress in AD-related models.

3.4. ICA shows potential PINK1 target engagement

Because *Pink1* was upregulated among mitophagy-related genes after ICA treatment, we examined whether ICA might act through a PINK1-associated mitophagy pathway. Docking analysis placed ICA in a putative binding pocket of PINK1, with predicted contacts involving Arg-544, Lys-552, Trp-378, Glu-370, and Lys-135 (Figs. 4A–4C). To assess the stability of this predicted complex, we performed a 100-ns molecular dynamics simulation. The RMSD profile showed that the complex reached equilibrium after approximately 20 ns and then fluctuated around 0.61 nm, indicating a relatively stable binding conformation during the simulation (Fig. 4D). The radius of gyration showed only minor variation, suggesting limited changes in the overall compactness of the complex (Fig. 4E). Hydrogen-bond analysis showed that ICA formed 0–8 hydrogen bonds with PINK1 during the simulation, with approximately four hydrogen bonds present in many frames (Fig. 4F). The RMSF profile further showed that most residues fluctuated below 1.0 nm, although several flexible regions displayed higher mobility (Fig. 4G). Gibbs free-energy landscape analysis indicated that the ICA-PINK1 complex sampled low-energy conformational states (Fig. 4H). Consistently, MM/PBSA analysis suggested a favorable predicted binding profile, with a calculated total binding free energy of −11.46 kcal·mol^{-1} (Fig. 4I). We next performed a cellular thermal shift assay to determine whether ICA affected PINK1 stability in cells. Compared with control cells, ICA-treated cells retained higher levels of soluble PINK1 at elevated temperatures, indicating increased thermal stability of PINK1 after ICA exposure (Figs. 4J and 4K). Together, these computational and cellular data support potential engagement of ICA with PINK1 and suggest that PINK1 may serve as an upstream target involved in ICA-induced mitophagy.

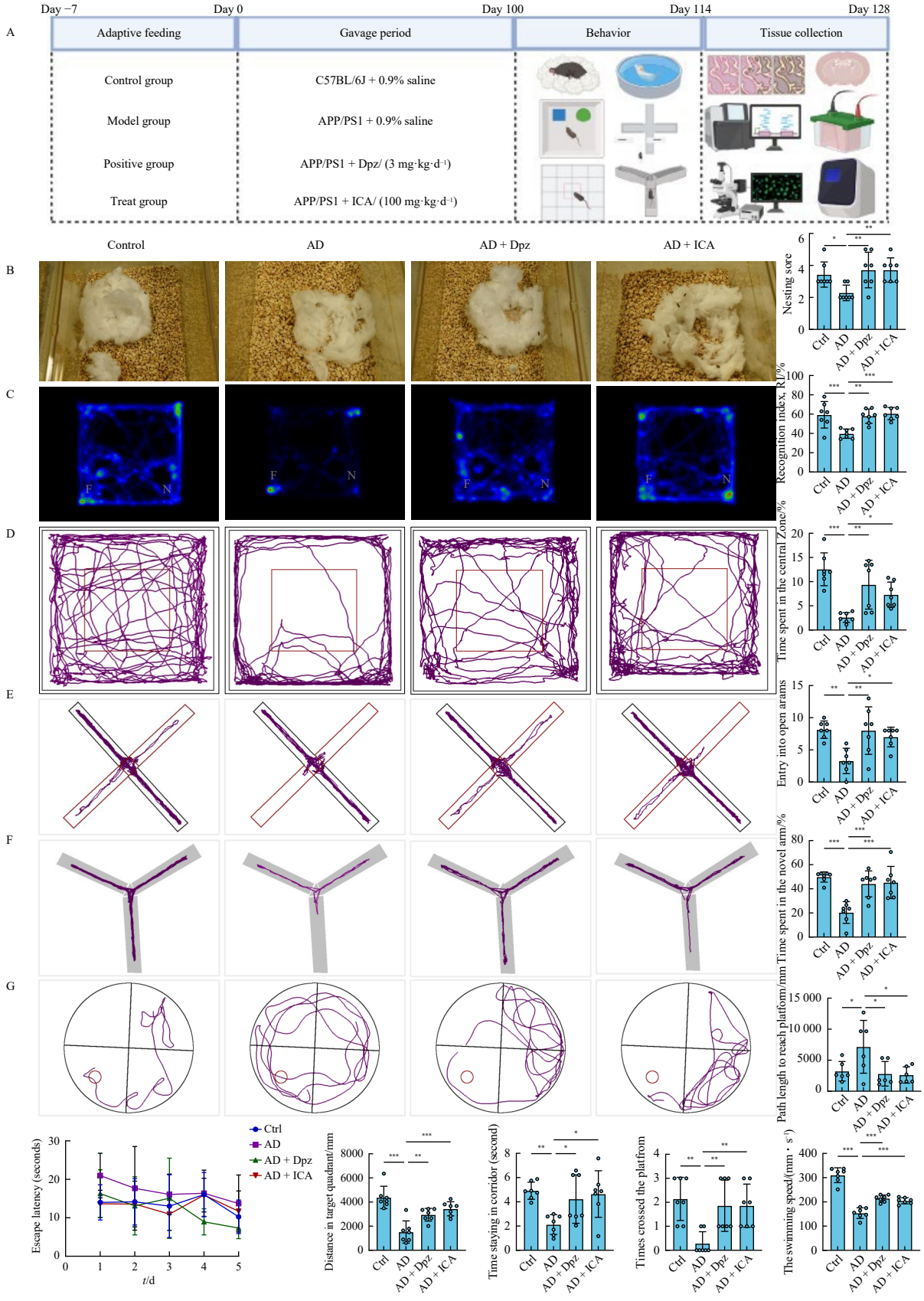


Fig. 1 ICA improves cognitive impairment in APP/PS1 mice. (A) Schematic diagram of the experimental design. (B) Representative images of nest-building behavior and quantification of nest-building scores. (C) Representative movement traces in the novel object recognition test and quantification of the recognition index. F, familiar object; N, novel object. (D) Representative locomotor trajectories in the open field test and quantification of time spent in the center zone. (E) Representative trajectories in the elevated plus maze and quantification of time spent in the open arms. (F) Representative trajectories in the Y-maze test and quantification of spontaneous novel-arm exploration. (G) Representative swim paths in the Morris water maze probe trial and quantification of escape latency during the acquisition phase, distance traveled, time spent in the target quadrant, platform crossings, and swimming speed during the probe trial. Data are presented as mean ± SD (n = 7 mice per group). Panels B–F and the probe-trial parameters in panel G were analyzed using one-way ANOVA followed by Bonferroni's post hoc test. Escape latency during the MWM acquisition phase in panel G was analyzed using two-way ANOVA followed by Bonferroni's multiple-comparisons test. $^{*}P < 0.05$, $^{**}P < 0.01$, $^{***}P < 0.001$ *vs* the AD group.

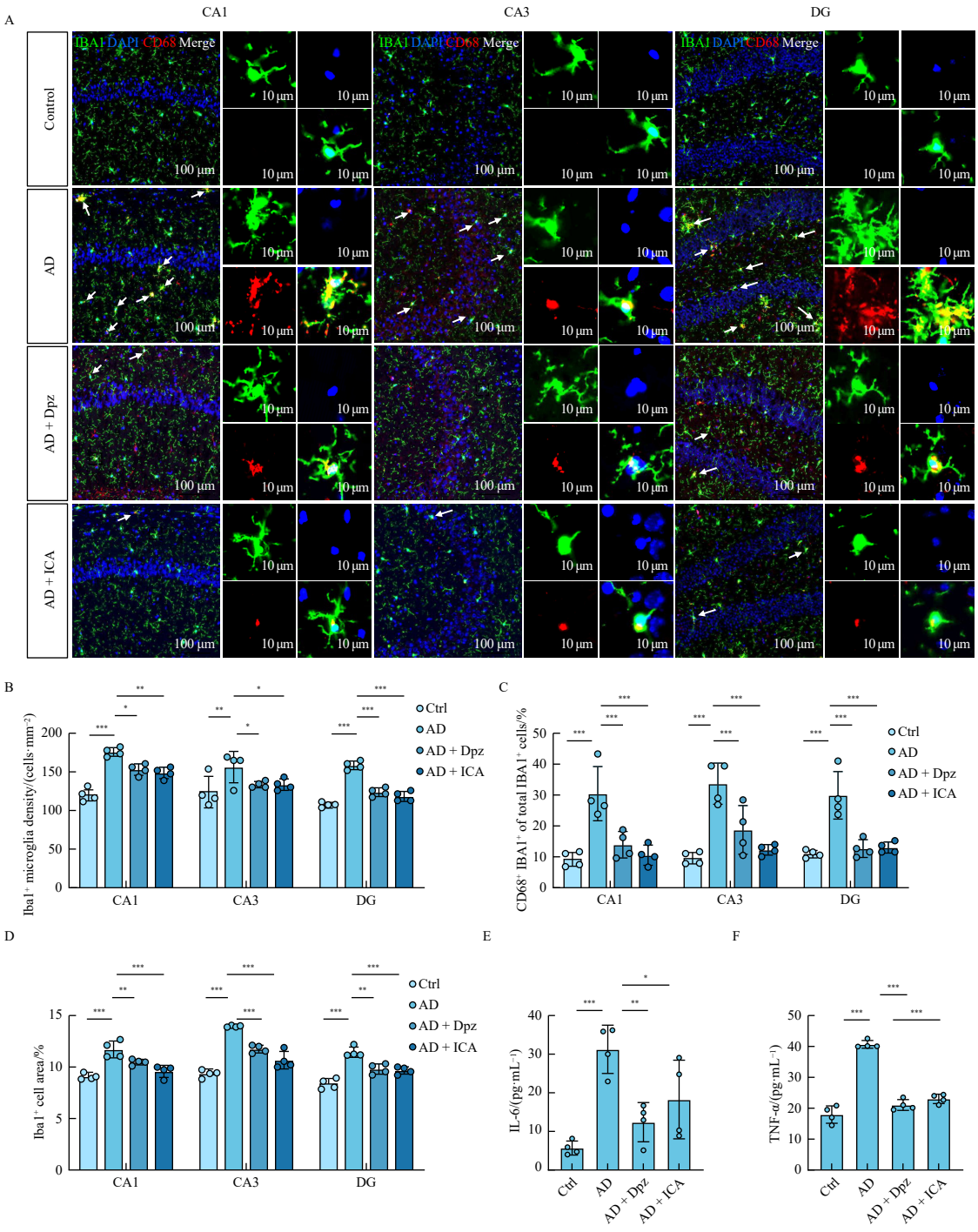


Fig. 2 ICA attenuates microglial activation and reduces pro-inflammatory markers in the hippocampus. (A) Representative confocal images of IBA1 and CD68 in the hippocampal CA1, CA3, and DG regions in the indicated groups. High-magnification images of the boxed areas and the corresponding single-channel images are shown on the right. White arrows indicate IBA1$^+$CD68$^+$ cells. Scale bars: 100 μm (overview) and 10 μm (magnified views). (B–D) Quantification of IBA1$^+$ microglial density, CD68$^+$IBA1$^+$/total IBA1$^+$ cells (%), and IBA1$^+$ area fraction (%) in the hippocampal CA1, CA3, and DG regions. (E, F) ELISA quantification of IL-6 and TNF-α levels in hippocampal tissue. Data are presented as mean ± SD (n = 4 for A–D; n = 3 for E and F). Quantitative data were analyzed using one-way ANOVA followed by Bonferroni's post hoc test. $^*P < 0.05$, $^{**}P < 0.01$, $^{***}P < 0.001$ *vs* the AD group.

3.5. ICA suppresses NLRP3/GSDMD-related pyroptotic changes in APP/PS1 mice and Aβ$_{1-42}$-stimulated BV-2 microglia

Because ICA enhanced mitophagy and reduced mitochondrial stress, we next examined whether these effects were accompanied by attenuation of NLRP3/GSDMD-related pyroptotic signaling, an inflammatory cell-death pathway closely linked to mitochondrial damage [15, 34]. In the hippocampus of APP/PS1 mice, the mRNA levels of *Nlrp3*, *Asc*, *Caspase-1*, and *Il-1β* were markedly higher than those in WT controls ($P < 0.01$), whereas ICA treatment reduced the expression of these genes ($P < 0.05$) (Fig. S2A). Dual IF staining also showed an increased proportion of NLRP3-positive microglia in APP/PS1 mice ($P < 0.01$), which was attenuated by ICA treatment ($P < 0.01$) (Figs. 5A and 5B, Fig. S2B). These findings suggest that ICA reduces hippocampal NLRP3 inflammasome-related activation in APP/PS1 mice.

We then assessed downstream pyroptosis-related changes. TEM showed pyroptosis-like ultrastructural abnormalities and membrane discontinuities in hippocampal tissue from APP/PS1 mice, whereas these pathological changes were less evident after

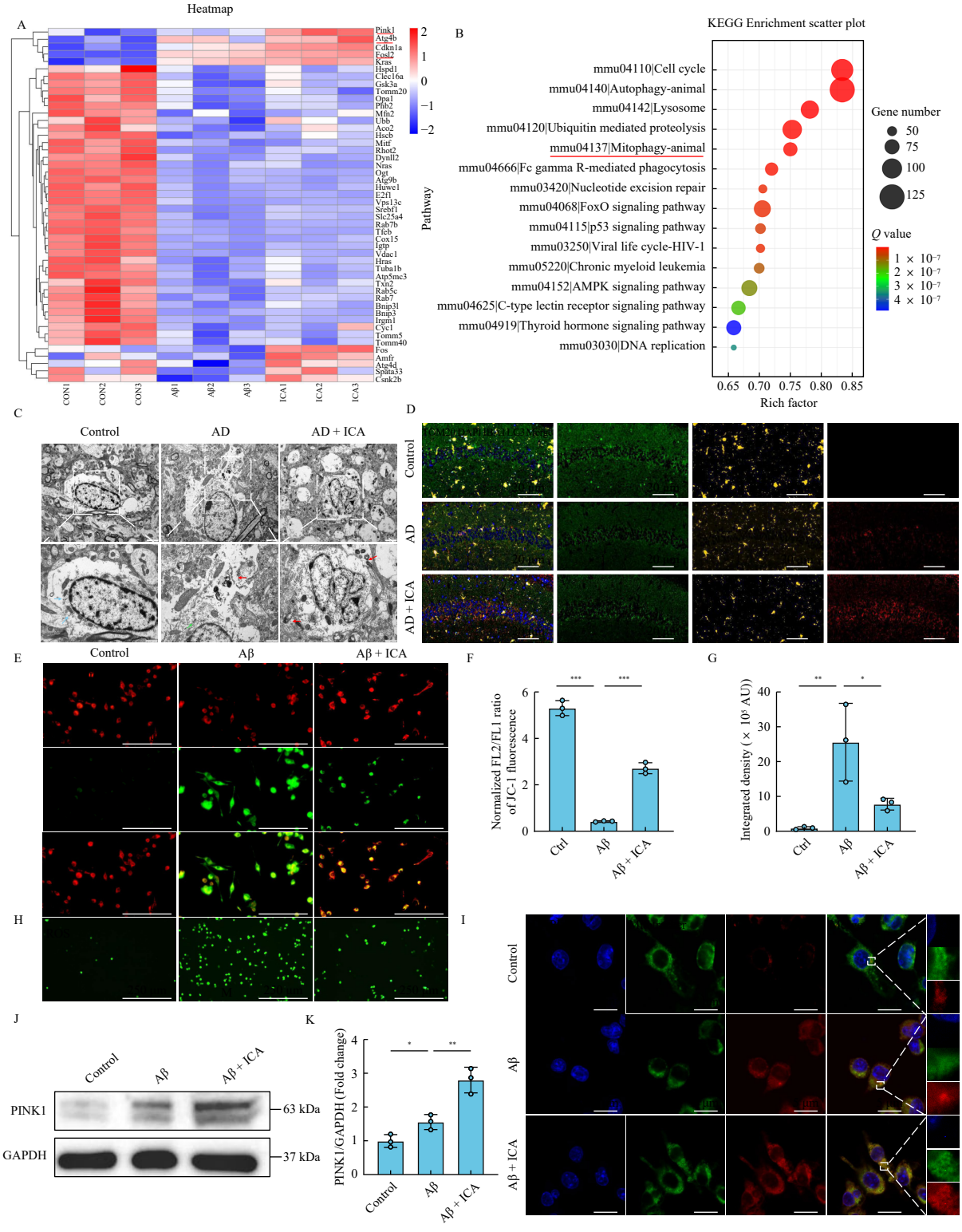


Fig. 3 ICA promotes mitophagy *in vivo* and restores mitochondrial function in Aβ-treated BV-2 microglia. (A) Heatmap of differentially expressed genes (DEGs) in hippocampal tissue from the Control, AD, and AD + ICA groups. (B) Kyoto Encyclopedia of Genes and Genomes (KEGG) enrichment analysis of DEGs. (C) Representative transmission electron microscopy (TEM) images showing mitochondrial morphology and autophagosome-like ultrastructural changes in hippocampal cells under different treatments. (D) Representative immunofluorescence images of TOM20, DAPI, IBA1, and LC3 in the hippocampus of the three groups. (E) Representative JC-1 staining images of BV-2 microglia showing JC-1 aggregates (red) and monomers (green). (F) Quantification of mitochondrial membrane potential by the normalized JC-1 FL2/FL1 fluorescence ratio. (G, H) Quantification and representative images of intracellular ROS levels in BV-2 microglia. (I) Representative confocal images showing LC3 and MitoTracker staining in BV-2 microglia. (J) Representative Western blot bands showing PINK1 protein expression in BV-2 microglia. (K) Quantification of PINK1 protein expression normalized to GAPDH and expressed as fold change relative to the Control group. Data are presented as mean ± SD (n = 3 for A–C, E–H and J–K, n = 4 for D, I). One-way ANOVA followed by Bonferroni's post hoc test was used for multiple-group comparisons. $^{*}P < 0.05$, $^{**}P < 0.01$, $^{***}P < 0.001$.

ICA treatment (Fig. 5C). Co-staining of GSDMD with NeuN, IBA1, and GFAP indicated that GSDMD immunoreactivity was mainly associated with IBA1-positive microglia rather than NeuN-positive neurons or GFAP-positive astrocytes (Fig. 5D). Consistently, the proportion of GSDMD-positive microglia was increased in APP/PS1 mice ($P < 0.001$) and was reduced after ICA treatment ($P < 0.001$) (Figs. 5E and 5F, Fig. S2C). Hippocampal LDH release and the levels of IL-1β and IL-18 were also elevated in APP/PS1

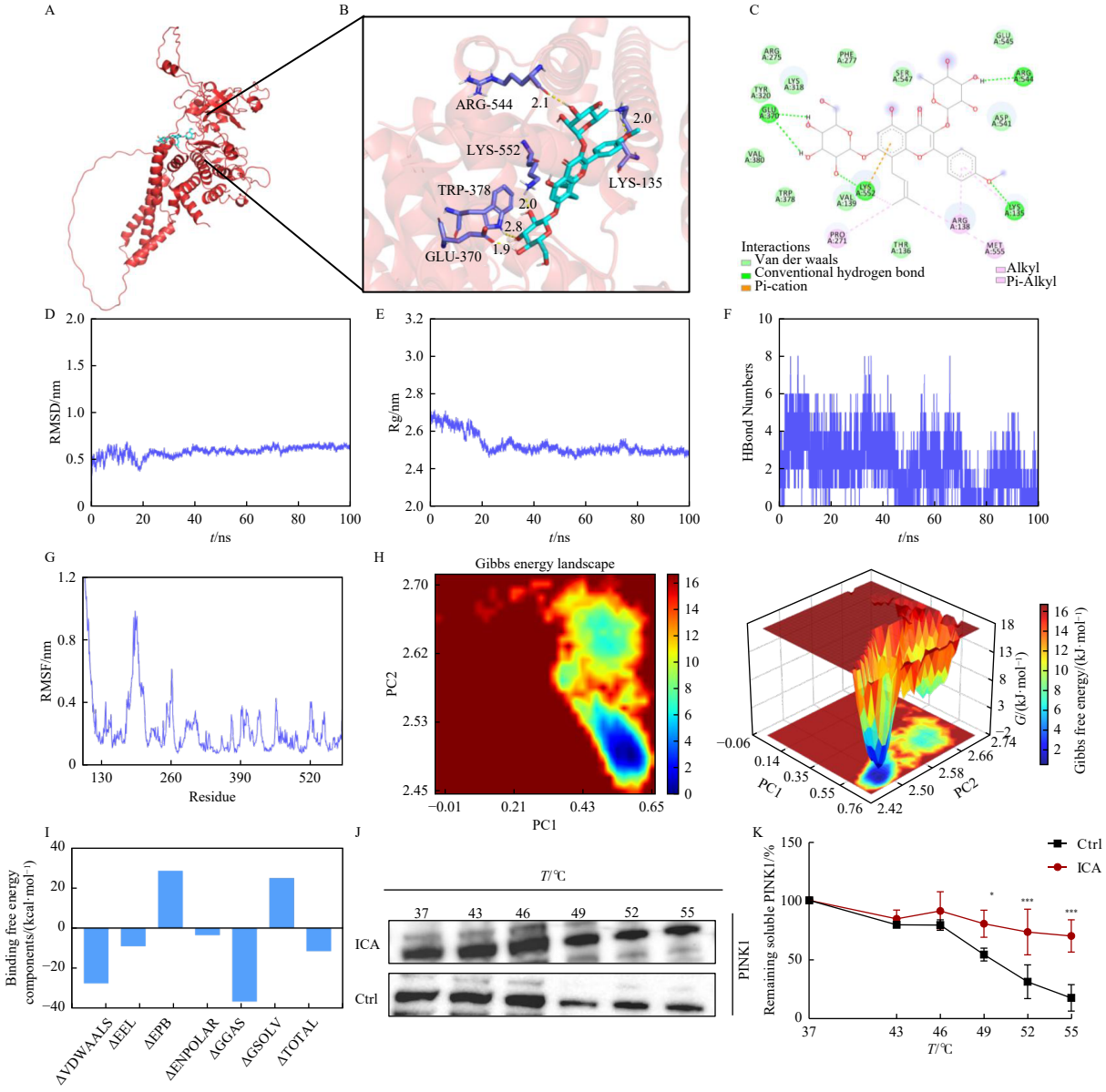


Fig. 4 ICA shows potential PINK1 target engagement. (A) Overall docking model showing the predicted binding pose of ICA in the PINK1 protein structure. (B) Enlarged view of the putative ICA-binding pocket in PINK1, with key interacting residues and predicted hydrogen-bond distances labeled. (C) Two-dimensional interaction map showing predicted contacts between ICA and PINK1, including hydrogen bonds, π-related interactions, and van der Waals interactions. (D) RMSD profile of the ICA-PINK1 complex during the 100-ns molecular dynamics simulation. The complex reached equilibrium after approximately 20 ns and then fluctuated around 0.61 nm. (E) Radius of gyration (Rg) profile showing minor changes in the compactness of the ICA-PINK1 complex during the simulation. (F) Number of hydrogen bonds formed between ICA and PINK1 during the 100-ns simulation. Hydrogen-bond numbers ranged from 0 to 8, with approximately four hydrogen bonds observed in many frames. (G) RMSF profile showing residue-level flexibility of PINK1 in the ICA-PINK1 complex, with most residues fluctuating below 1.0 nm. (H) Two-dimensional and three-dimensional Gibbs free-energy landscapes of the ICA-PINK1 complex. Blue regions indicate lower-energy conformational states. (I) MM/PBSA binding free-energy component analysis of the ICA-PINK1 complex. The calculated total binding free energy was −11.46 kcal·mol^{-1}. (J) Representative cellular thermal shift assay immunoblots showing remaining soluble PINK1 in BV-2 cells treated with Ctrl or ICA at the indicated temperatures. (K) Quantification of soluble PINK1 levels in the cellular thermal shift assay. Band intensities were normalized to the 37 °C sample within each group. Data are presented as mean ± SD from three independent experiments. Statistical significance was determined by two-way ANOVA with Bonferroni's multiple-comparisons test. $^{*}P < 0.05$ and $^{***}P < 0.001$ *vs* Ctrl at the same temperature.

mice ($P < 0.001$), while ICA significantly decreased these pyroptosis-related inflammatory readouts ($P < 0.001$) (Figs. 5G–5I). Together, these results indicate that ICA attenuates microglia-associated pyroptotic changes and inflammatory cytokine release in APP/PS1 mice.

To extend these observations *in vitro*, $A\beta_{1-42}$-stimulated BV-2 microglia were treated with ICA, with MCC950 used as an NLRP3 inhibitor control. CCK-8 assays showed that $A\beta_{1-42}$ reduced cell viability ($P < 0.001$), whereas ICA and MCC950 partially restored cell viability ($P < 0.01$) (Figs. S2D–S2E). Light microscopy showed that $A\beta_{1-42}$-induced cell swelling and membrane blebbing were less evident after ICA treatment (Fig. S3A). PI staining further showed that ICA and MCC950 reduced the proportion of PI-positive cells ($P < 0.05$) (Figs. S3B and S3D). Because ASC speck formation reflects inflammasome assembly, we next examined ASC distribution by IF. $A\beta_{1-42}$ markedly increased ASC speck formation, whereas ICA and MCC950 reduced the proportion of ASC speck-positive cells ($P < 0.05$) (Figs. S3C and S3E). ELISA showed that ICA decreased $A\beta_{1-42}$-induced IL-1β and IL-18 secretion ($P < 0.05$) (FigS. S3F and S3G). Western blotting further showed that ICA reduced the $A\beta_{1-42}$-induced upregulation of NLRP3 and pro-Caspase-1 ($P < 0.05$) (Figs. S3H–S3J). Consistently, ICA markedly decreased $A\beta_{1-42}$-induced LDH release ($P < 0.001$) (Fig. S3K). These *in vivo* and *in vitro* findings indicate that ICA suppresses NLRP3 inflammasome-associated inflammatory injury and GSDMD-related pyroptotic changes in AD-related models. We further examined the relevance of this pathway to human AD using the hippocampal transcriptomic dataset GSE36980. *NLRP3* ex-

pression was higher in AD patients than in controls ($P < 0.01$) (Figs. 5J and 5K). *IL18R1* and *GSDMD* expression were also increased in AD hippocampal tissue ($P < 0.05$) (Figs. 5L and 5M). These human transcriptomic data support the pathological relevance of NLRP3/GSDMD-related pyroptotic signaling in AD.

3.6. Pink1 knockdown weakens ICA-induced mitophagy and attenuates ICA-mediated suppression of NLRP3 inflammasome-associated inflammatory injury

To assess whether PINK1 was involved in the effects of ICA on mitophagy and downstream inflammatory injury, we first screened two siRNAs targeting *Pink1* in $A\beta_{1-42}$-stimulated BV-2 microglia. Both si-PINK1-1 and si-PINK1-2 reduced PINK1 expression at the protein and mRNA levels, with si-PINK1-2 showing the stronger knockdown efficiency (Figs. 6A–6C). si-PINK1-2 was therefore used in the following experiments.

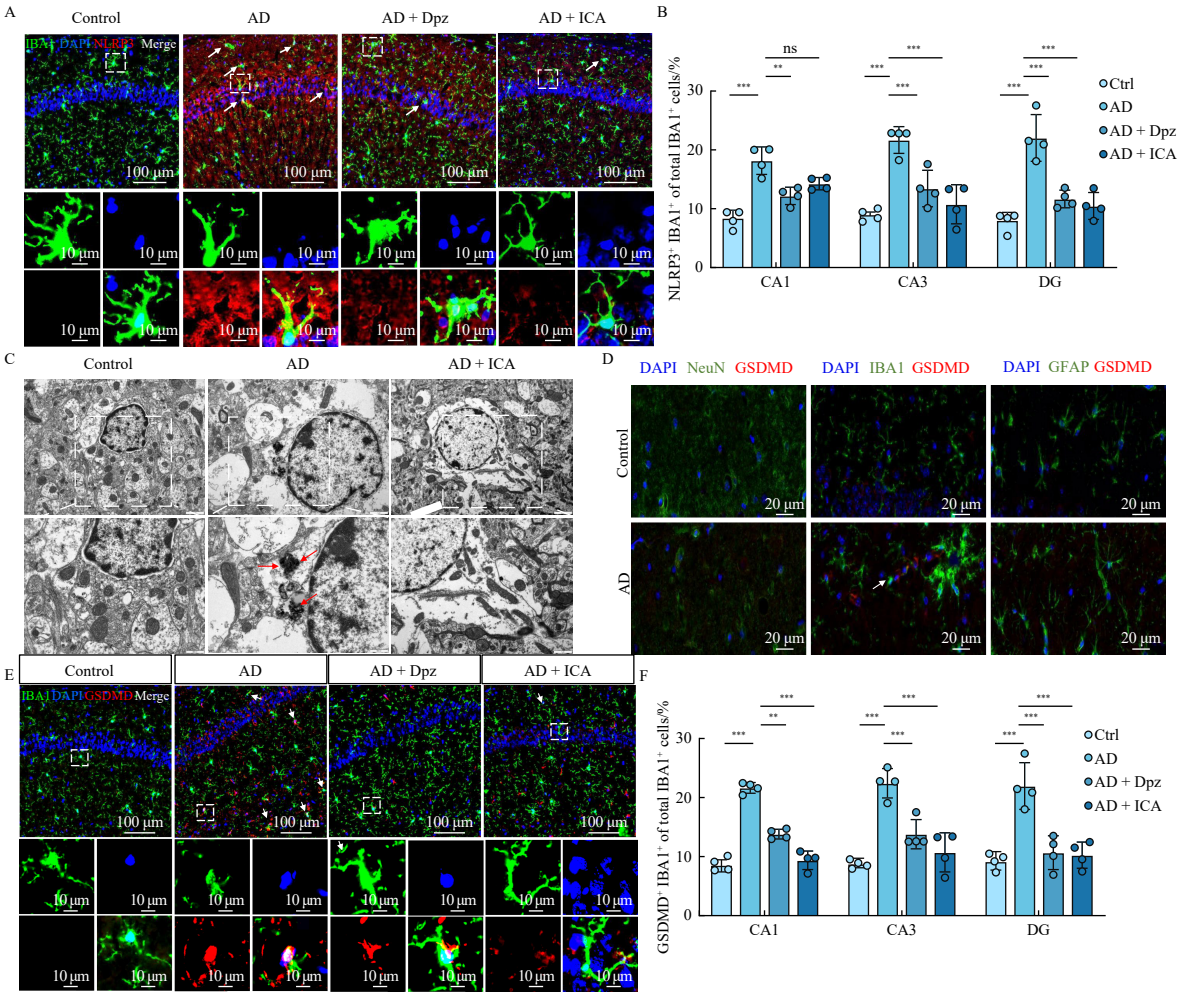
We next examined whether *Pink1* knockdown affected the regulatory effect of ICA on NLRP3 inflammasome-associated inflammatory markers. Under $A\beta_{1-42}$ stimulation, ICA increased PINK1 expression in siNC-transfected cells, whereas this effect was markedly weakened after *Pink1* knockdown (Figs. 6D and 6J). ICA also reduced the $A\beta_{1-42}$-induced upregulation of NLRP3, pro-Caspase-1, mature IL-18, and mature IL-1β in siNC-transfected BV-2 microglia, and these inhibitory effects were partially reversed by PINK1 knockdown (Figs. 6D, 6E, 6G–6I). Changes in GSDMD-FL were also observed under ICA treatment and *Pink1* knockdown conditions, supporting the involvement of GSDMD-related protein changes in this process (Figs. 6D and 6F).

We then assessed mitophagy by LC3 and TOM20 co-staining. In siNC-transfected cells, ICA increased LC3/TOM20 colocalization under $A\beta_{1-42}$ stimulation. This effect was reduced after *Pink1* knockdown (Figs. 6K and 6L), indicating that PINK1 contributes to ICA-induced mitophagy in $A\beta_{1-42}$-stimulated BV-2 microglia. Together, these findings suggest that PINK1 is involved, at least in part, in the ability of ICA to enhance mitophagy and suppress NLRP3 inflammasome-associated inflammatory injury and GSDMD-related pyroptotic changes.

3.7. Mdivi-1 co-treatment attenuates the protective effects of ICA on microglia-associated pyroptosis and neuroinflammation

To further evaluate whether mitophagy contributed to the protective effects of ICA, APP/PS1 mice were co-treated with Mdivi-1. We first examined whether Mdivi-1 affected the mitophagy-related changes induced by ICA. IF co-staining of IBA1, LC3, and TOM20 showed that ICA increased LC3 fluorescence intensity, enhanced LC3/TOM20 colocalization, and promoted LC3/TOM20 colocalization within IBA1-positive microglia. These changes were attenuated in the presence of Mdivi-1 (Figs. 7A and 7B), indicating that pharmacological inhibition partially impaired the mitophagy-related effects of ICA. We next evaluated whether these changes were accompanied by altered pyroptosis-related markers. Dual IF staining for IBA1 and GSDMD showed that ICA markedly reduced the proportion of $GSDMD^+$ microglia ($GSDMD^+IBA1^+/IBA1^+$) ($P < 0.05$). However, this reduction was significantly attenuated when ICA was combined with Mdivi-1, resulting in a higher proportion of $GSDMD^+$ microglia than ICA alone ($P < 0.05$) (Figs. 7C and 7D).

Consistent with this, LDH release assays demonstrated that



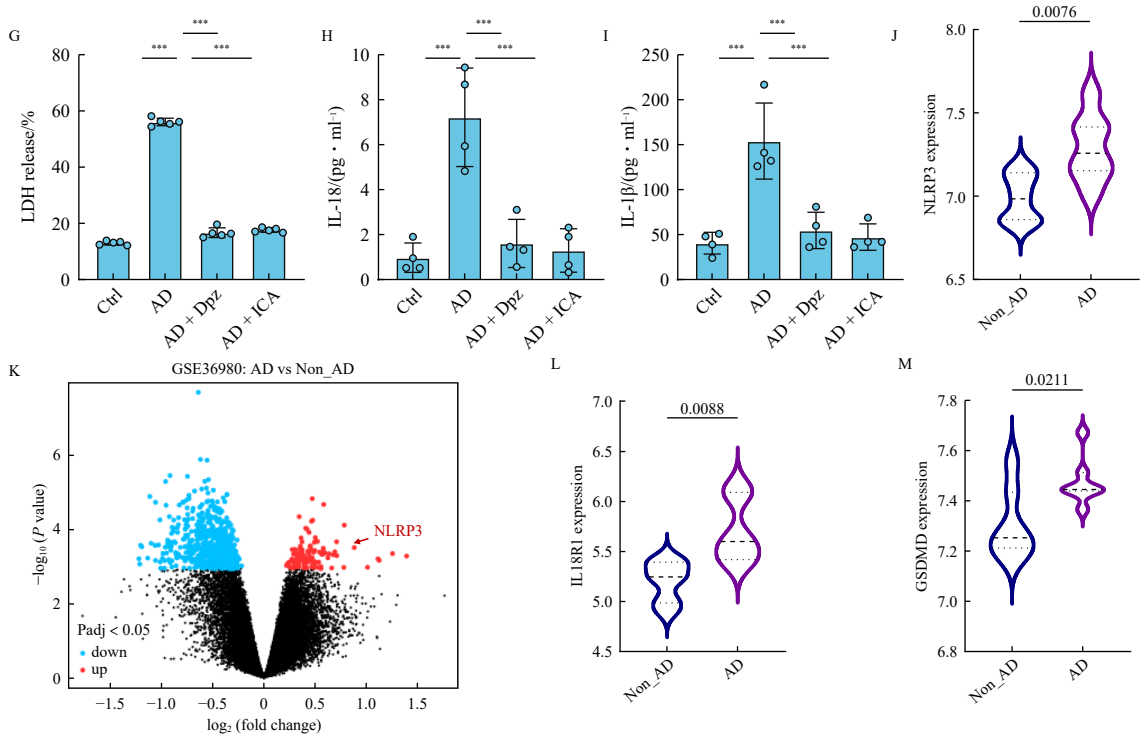


Fig. 5 ICA suppresses NLRP3/GSDMD-related pyroptotic changes in APP/PS1 mice. (A) Representative confocal images of IBA1 (green), DAPI (blue), and NLRP3 (red) in the hippocampal CA1 regions of the indicated groups. High-magnification images of the boxed areas and the corresponding single-channel images are shown on the right. White arrows indicate NLRP3$^+$IBA1$^+$ cells. Scale bars: 100 μm (overview) and 10 μm (magnified views). (B) Quantitative analysis of NLRP3$^+$IBA1$^+$ / total IBA1$^+$ cells (%) in the hippocampal CA1, CA3, and DG regions. (C) Representative TEM images showing pyroptosis-related ultrastructural changes in hippocampal cells from the Control, AD, and AD + ICA groups. Red arrows indicate representative ultrastructural abnormalities associated with pyroptotic injury. (D) Representative immunofluorescence images of NeuN, IBA1, or GFAP (green), together with GSDMD (red) and DAPI (blue) in the hippocampus. White arrows indicate GSDMD$^+$IBA1$^+$ cells. Scale bar: 20 μm. (E) Representative confocal images of IBA1 (green), DAPI (blue), and GSDMD (red) in the hippocampal CA1 regions of the indicated groups. High-magnification images of the boxed areas and the corresponding single-channel images are shown on the right. White arrows indicate GSDMD$^+$IBA1$^+$ cells. Scale bars: 100 μm (overview) and 10 μm (magnified views). (F) Quantitative analysis of GSDMD$^+$IBA1$^+$/total IBA1$^+$ cells (%) in the hippocampal CA1, CA3, and DG regions. (G) Lactate dehydrogenase release in hippocampal tissue in the indicated groups. (H, I) ELISA quantification of IL-18 and IL-1β levels in hippocampal tissue. (J, K) Analysis of *NLRP3* expression in hippocampal tissue from patients with AD and non-AD controls in the GSE36980 dataset. (L, M) Violin plots showing *IL18R1* and *GSDMD* expression in hippocampal tissue from AD and non-AD individuals in the GSE36980 dataset. Data are presented as mean ± SD (n = 4 for A–F and H-I; n = 5 for G; AD, n = 7; non-AD, n = 10 for J–M). Panels B–I were analyzed using one-way ANOVA followed by Bonferroni's post hoc test. Panels J–M were analyzed by unpaired two-tailed Student's t-test. $^*P < 0.05$, $^{**}P < 0.01$, $^{***}P < 0.001$ *vs* the AD group.

ICA markedly decreased LDH release in APP/PS1 mice (P < 0.001), whereas co-administration of Mdivi-1 significantly increased LDH release relative to ICA treatment alone (P < 0.001) (Fig. 7E). Western blotting of hippocampal tissues further showed that ICA reduced the levels of NLRP3, GSDMD, pro-Caspase-1, mature IL-18, and mature IL-1β in APP/PS1 mice, whereas Mdivi-1 co-treatment partially reversed these inhibitory effects (Fig. 7F, Fig. S2F). Furthermore, ELISA results showed that ICA substantially reduced the levels of TNF-α, IL-6, IL-18, and IL-1β (P < 0.001), whereas Mdivi-1 co-treatment significantly elevated these cytokines (P < 0.01) (Figs. 7G–7J). Together, these findings indicate that Mdivi-1 co-treatment attenuates ICA's ability to suppress microglia-associated pyroptosis and inflammatory cytokine release.

3.8. ICA demonstrates a favorable safety profile during long-term administration

To assess the safety of prolonged ICA administration, H&E staining was performed on major organs, including the heart, liver, spleen, lungs, and kidneys. Compared with control mice, ICA-treated APP/PS1 mice showed no evidence of inflammatory infiltration, cellular necrosis, or structural tissue damage. Overall tissue architecture remained intact across all examined organs (Fig. S4A). Serum biochemical analyses further demonstrated that liver function markers (ALT, AST) and renal function indicators (CREA, urea) were not significantly altered following ICA treatment (P > 0.05). In addition, complete blood count analyses revealed no significant changes in WBC, RBC, HGB, or HCT levels compared with the control group (P > 0.05) (Figs. S4B–S4C). These results indicate that long-term ICA administration does not induce detectable organ toxicity or hematologic abnormalities, supporting the favorable tolerability and safety of chronic ICA exposure *in vivo*.

4. Discussion

This study, using APP/PS1 mice and an A$\beta_{1\text{-}42}$-induced BV-2 microglial model, shows that ICA enhances PINK1-associated mitophagy and attenuates NLRP3/GSDMD-related microglial pyroptotic injury, accompanied by improved behavioral performance in APP/PS1 mice. In the MWM, ICA shortened escape latency and improved probe trial performance. APP/PS1 mice exhibited reduced swimming speed relative to WT controls, and ICA partially increased swimming speed; therefore, acquisition-phase parameters such as escape latency should be interpreted with caution. Notably, ICA also significantly improved probe trial indices and showed consistent benefits across independent behavioral paradigms, including nest-building, NOR, and Y-maze tests. Collectively, these findings support the view that ICA improves cognitive-related behavioral performance while modulating mitochondrial homeostasis and neuroinflammatory signaling in AD-related settings.

Previous studies have indicated that microglia in AD exhibit a chronically activated, pro-inflammatory state characterized by retracted processes, enlarged cell bodies, marked upregulation of the phagocytic lysosomal marker CD68, and robust secretion of pro-inflammatory cytokines [5]. These alterations are closely associated with cognitive decline. In line with these observations, we also found a significant increase in IBA1$^+$CD68$^+$ microglia in the

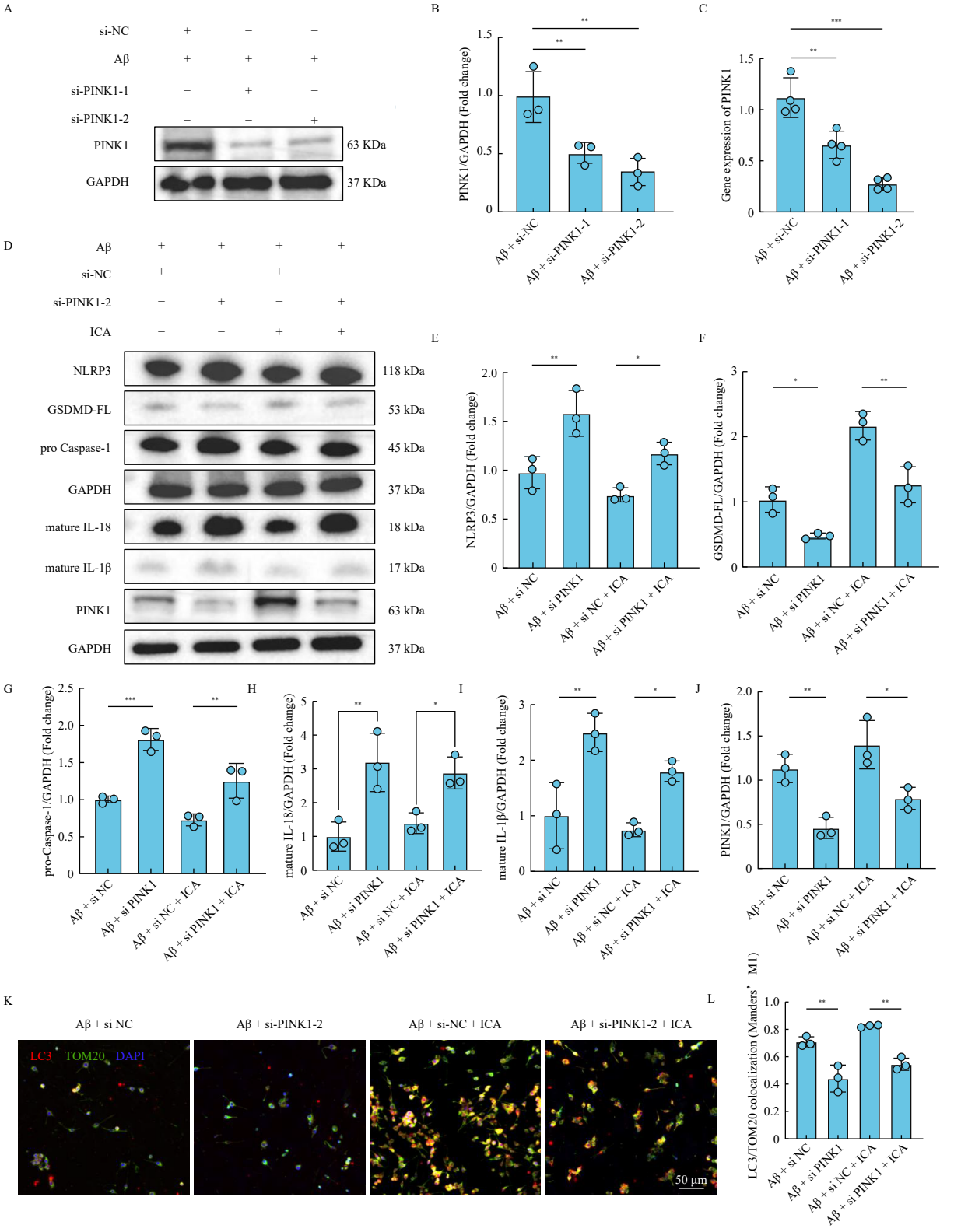


Fig. 6 *Pink1* knockdown weakens ICA-induced mitophagy and attenuates ICA-mediated suppression of NLRP3 inflammasome-associated inflammatory injury in $A\beta_{1-42}$-stimulated BV-2 microglia. (A) Representative Western blot bands showing PINK1 protein expression in $A\beta_{1-42}$-stimulated BV-2 microglia transfected with siNC, si-PINK1-1, or si-PINK1-2. GAPDH was used as the loading control. (B) Quantification of PINK1 protein expression normalized to GAPDH. (C) RT-qPCR analysis of *Pink1* mRNA expression after siRNA transfection. (D) Representative Western blot bands showing NLRP3, GSDMD-FL, pro-Caspase-1, mature IL-18, mature IL-1β, and PINK1 protein levels in $A\beta_{1-42}$-stimulated BV-2 microglia treated with siNC, si-PINK1-2, ICA, or their combination. GAPDH was used as the loading control. (E–J) Quantification of NLRP3, GSDMD-FL, pro-Caspase-1, mature IL-18, mature IL-1β, and PINK1 protein levels normalized to GAPDH. (K) Representative fluorescence images showing LC3 (red), TOM20 (green), and DAPI (blue) staining in the indicated groups. Scale bar: 50 μm. (L) Quantification of LC3/TOM20 colocalization using Manders' M1 coefficient. Data are presented as mean ± SD (n = 3 for panels B and E–J and L; n = 4 for panel C). Statistical significance was determined by one-way ANOVA followed by Bonferroni's post hoc test. $^{*}P < 0.05$, $^{**}P < 0.01$, $^{***}P < 0.001$.

hippocampus of APP/PS1 mice, accompanied by markedly elevated IL-6 and TNF-α levels, confirming a highly activated microglial state in this AD model. Notably, ICA intervention significantly reduced microglial density, suppressed CD68 upregulation, and decreased inflammatory cytokine release, suggesting that ICA effectively alleviates the neuroinflammatory microenviron-

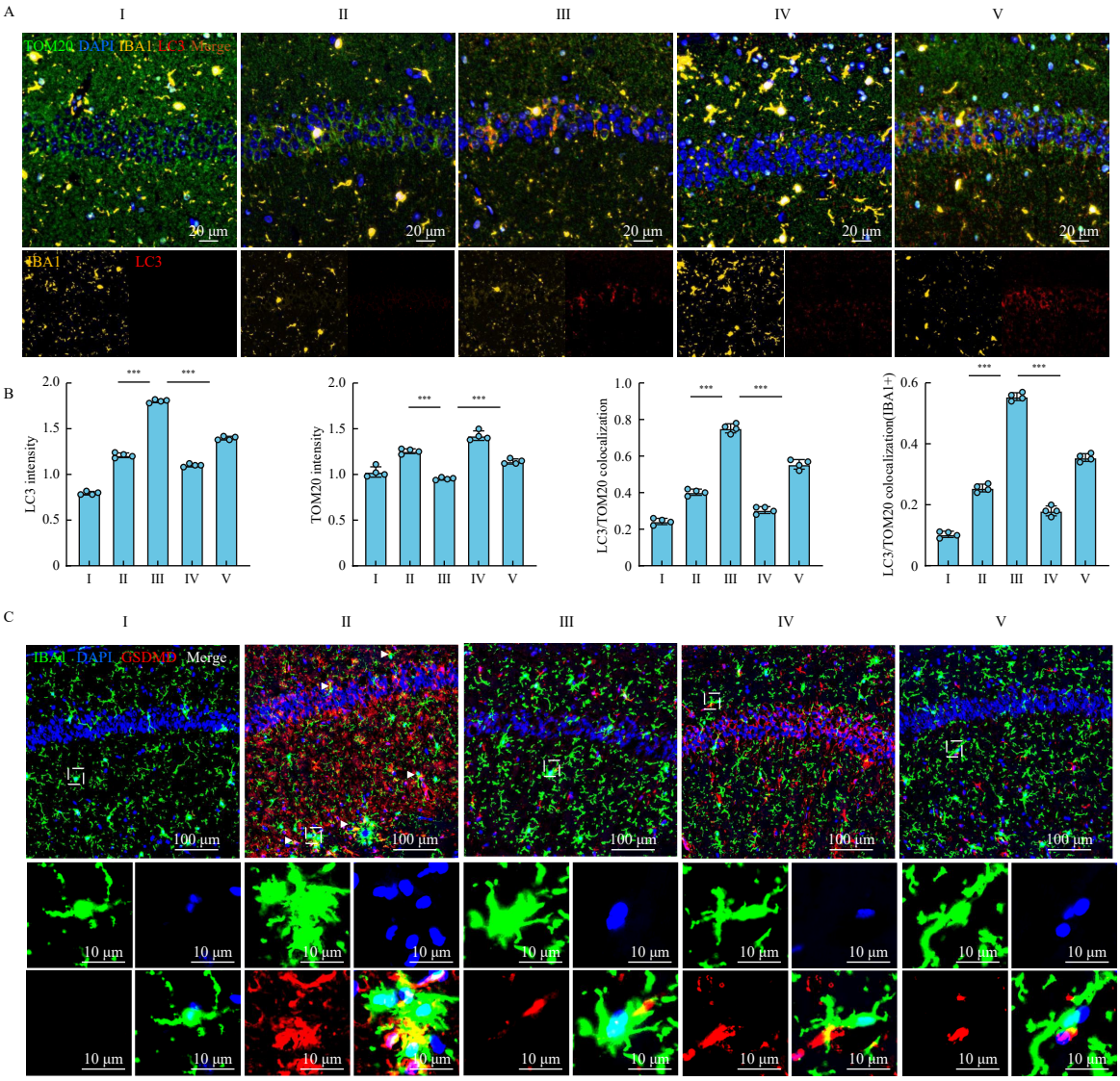
ment associated with AD. Building on prior reports that ICA modulates neuroinflammation through signaling pathways such as AKT1, NF-κB, and TNF [19, 22, 35], our findings provide additional evidence supporting its anti-inflammatory effects through glial cell-state regulation, further reinforcing ICA's potential as a neuroinflammatory modulator.

Pyroptosis has become increasingly recognized as a key amplifying mechanism of neuroinflammation in AD [36, 37]. Preclinical studies consistently report elevated NLRP3 and activated GSDMD levels in brain tissue from AD patients and various AD models, indicating that inflammasome-driven pyroptosis is a critical contributor to AD pathological progression. In line with these findings, our study demonstrated marked upregulation of NLRP3, ASC, caspase-1, GSDMD, and their downstream inflammatory mediators in the hippocampus of APP/PS1 mice and in $A\beta_{1-42}$-stimulated BV-2 microglia. Notably, ICA intervention reduced these alterations, suggesting that ICA attenuates NLRP3 inflammasome-associated inflammatory responses and GSDMD-related pyroptotic changes.

Importantly, our findings identify mitophagy as an important upstream process associated with ICA modulation of inflammasome activation and pyroptosis. Extensive evidence indicates that mitochondrial injury, *via* excessive ROS production, is a major trigger of NLRP3 assembly, thereby driving neuroinflammation in AD [38-40]. Consistent with this mechanism, we observed that ICA markedly increased the expression of key mitophagy-related genes, reduced ROS accumulation, and promoted autophagosome formation. Notably, pharmacological disruption of mitophagy-related mitochondrial processes weakened ICA's ability to suppress NLRP3/GSDMD-related inflammatory injury. However, Mdivi-1 cannot be considered a highly specific or definitive inhibitor of mitophagy, and its effects may also involve mitochondrial fission-related or other non-mitophagy mechanisms. These findings underscore the central importance of maintaining mitochondrial homeostasis in mitigating neuroinflammation and slowing neurodegenerative progression.

Importantly, increased LC3-related signals alone do not necessarily indicate functionally enhanced mitophagy, because LC3 accumulation may also reflect altered autophagosome formation or impaired autophagic turnover. Therefore, LC3-based observations should be interpreted together with mitochondrial colocalization and, ideally, additional flux-related indicators such as p62. In this context, the possibility that ICA + Mdivi-1 may still show elevated LC3-related signals while downstream protective effects are attenuated suggests that LC3 accumulation does not necessarily equate to fully functional mitophagy and that Mdivi-1 may influence ICA-mediated protection through mitochondrial fission-related or other non-mitophagy mechanisms.

Notably, ICA has demonstrated robust neuroprotective effects across multiple neurological disease models [41-43]. Previous studies have shown that ICA can modulate key inflammatory signaling pathways, enhance synaptic function, mitigate oxidative



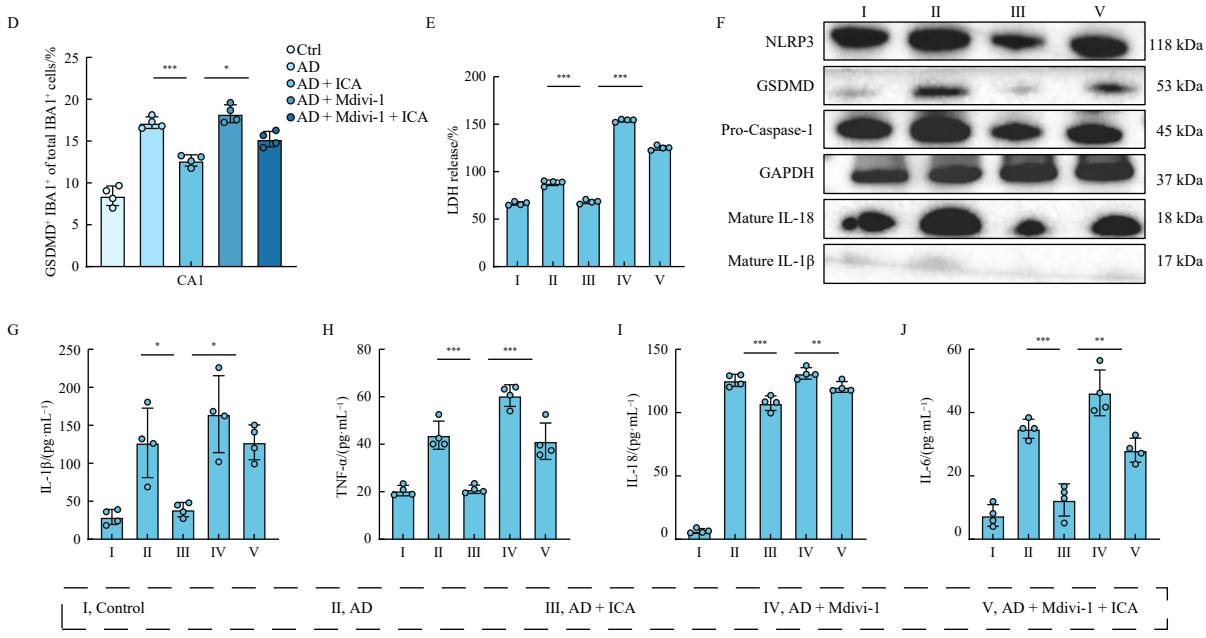


Fig. 7 Mitophagy inhibition attenuates protective effects of ICA on microglial pyroptosis and neuroinflammation in APP/PS1 mice. (A) Representative confocal images of TOM20 (green), DAPI (blue), IBA1 (yellow), and LC3 (red) in the hippocampus of five indicated groups. Representative single-channel images of IBA1 and LC3 are shown below. Scale bar: 20 μm. (B) Quantification of LC3 fluorescence intensity, TOM20 fluorescence intensity, LC3/TOM20 colocalization, and LC3/TOM20 colocalization within IBA1$^+$ microglia. (C) Representative confocal images of IBA1 (green), DAPI (blue), and GSDMD (red) in the hippocampus of the five indicated groups. High-magnification images of the boxed areas and the corresponding single-channel images are shown below. Scale bars: 100 μm (overview) and 10 μm (magnified views). (D) Quantification of GSDMD$^+$IBA1$^+$/total IBA1$^+$ cells (%) in the hippocampal CA1, CA3, and DG regions. (E) LDH release in hippocampal tissue in the indicated groups. (F) Representative Western blot bands showing the protein levels of NLRP3, GSDMD-FL, pro-Caspase-1, mature IL-18, and mature IL-1β in hippocampal tissues from selected groups (I, II, III, and V). GAPDH was used as the loading control. (G–J) ELISA quantification of IL-1β, TNF-α, IL-18, and IL-6 levels in the hippocampus. Group labels: I, Control; II, AD; III, AD + ICA; IV, AD + Mdivi-1; V, AD + Mdivi-1 + ICA. Data are presented as mean ± SD (n = 4). Panels B and D–J were analyzed using one-way ANOVA followed by Bonferroni's post hoc test. $^*P < 0.05$, $^{**}P < 0.01$, $^{***}P < 0.001$ *vs* the AD group, $^{\#}P < 0.05$, $^{\#\#}P < 0.01$, $^{\#\#\#}P < 0.001$ *vs* the AD + ICA group.

stress, and suppress pyroptosis in diverse pathological contexts [44, 45]. Building upon these findings, the present study further extends the mechanistic framework of ICA by positioning it as a regulator of the mitophagy-NLRP3/GSDMD inflammatory axis. Compared with highly selective NLRP3 inhibitors, which have encountered safety limitations in clinical development [46], ICA simultaneously improves mitophagy, restores mitochondrial homeostasis, and suppresses inflammasome activation. Moreover, ICA exhibited favorable tolerability during long-term administration in our study, reinforcing its translational potential. Collectively, these features indicate that ICA may offer a more advantageous multi-target therapeutic strategy for AD, particularly in conditions requiring chronic treatment and broad-spectrum modulation of pathological processes.

Despite the mechanistic insights provided in this study, several limitations should be acknowledged. First, mitophagy-related validation was primarily achieved using the pharmacological agent Mdivi-1, whose target specificity remains debated. Future studies using *in vivo*, cell-type-specific genetic models, such as microglia-specific *Pink1* deletion, will be needed to define the causal role of PINK1-associated mitophagy in ICA-mediated neuroprotection. Second, given the multifactorial nature of AD pathology, our work did not examine other key pathological processes, including tau hyperphosphorylation and synaptic dysfunction, which warrant further investigation to fully delineate ICA's therapeutic spectrum. Third, a WT + ICA group was not included in the present experimental design. As this study primarily aimed to evaluate ICA's therapeutic efficacy under AD-like pathological conditions, baseline effects under physiological conditions were not systematically assessed. Inclusion of such a group in future studies would provide a more comprehensive evaluation of ICA's potential modulatory effects in normal brain homeostasis. Fourth, this study utilized only male APP/PS1 mice, which may limit the generalizability of our findings; incorporating female animals in future experiments will be essential, particularly given known sex differences in AD susceptibility and neuroimmune responses. These issues should be addressed in future studies to support the translational development of ICA as a potential therapeutic agent for AD.

5. Conclusions

This study shows that ICA improves cognitive deficits in APP/PS1 mice, at least partly by enhancing PINK1-associated mitophagy and reducing NLRP3/GSDMD-related microglial pyroptotic injury. These findings support a model in which ICA improves mitochondrial quality control, limits mitochondrial stress, and subsequently dampens inflammasome-associated inflammatory responses in AD-related models. Together, our data suggest that ICA may be a promising pharmacological candidate for reducing microglia-driven neuroinflammation and slowing AD-related pathological progression (Fig. 8).

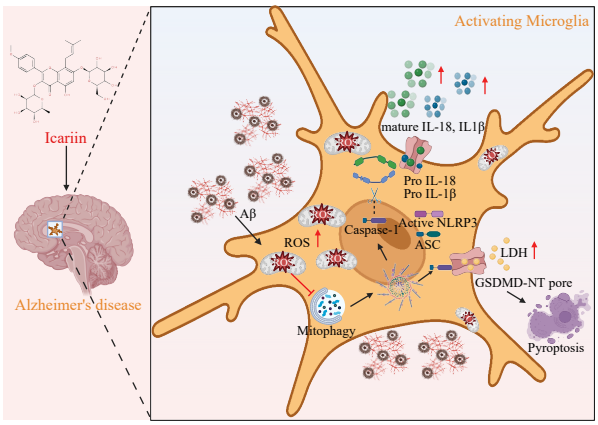


Fig. 8 Schematic representation of the proposed mechanism. Icariin enhances PINK1-associated mitophagy, reduces mitochondrial ROS accumulation, and attenuates NLRP3/GSDMD-related microglial pyroptotic injury, thereby improving AD-related cognitive and inflammatory phenotypes.

Funding

This work was fsupported by the National Natural Science Foundation of China (Nos. 82104967 and 82374552), the Natural Science Foundation of Hunan Province (No. 2022JJ40728), and the Scientific Research Launch Project for New Employees of the Second Xiangya Hospital of Central South University (QH20210442).

Supplementary data

Supplementary data associated with this article can be requested by sending E-mail to the corresponding authors.

Declaration of competing interest

The authors declare that they have no competing interests.

References

1 Graff-Radford J, Yong KXX, Apostolova LG, et al. New insights into atypical Alzheimer's disease in the era of biomarkers. *Lancet Neurol*. 2021;20(3):222-234. https://doi.org/10.1016/S1474-4422(20)30440-3.
2 2024 Alzheimer's disease facts and figures. *Alzheimers Dement*. 2024;20(5):3708-3821. https://doi.org/10.1002/alz.13809.
3 Ren RL, Qi JL, Lin SH, et al. The China Alzheimer report 2022. *Gen Psychiatr*. 2022;35(1):e100751. https://doi.org/10.1136/gpsych-2022-100751.
4 Mangialasche F, Solomon A, Winblad B, et al. Alzheimer's disease: clinical trials and drug development. *Lancet Neurol*. 2010;9(7):702-716. https://doi.org/10.1016/S1474-4422(10)70119-8.
5 Calsolaro V, Edison P. Neuroinflammation in Alzheimer's disease: current evidence and future directions. *Alzheimers Dement*. 2016;12(6):719-732. https://doi.org/10.1016/j.jalz.2016.02.010.
6 Singh D. Astrocytic and microglial cells as the modulators of neuroinflammation in Alzheimer's disease. *J Neuroinflamm*. 2022;19:206. https://doi.org/10.1186/s12974-022-02565-0.
7 Deczkowska A, Amit I, Schwartz M. Microglial immune checkpoint mechanisms. *Nat Neurosci*. 2018;21(6):6. https://doi.org/10.1038/s41593-018-0145-x.
8 Fu W, Vukojevic V, Patel A, et al. Role of microglial amylin receptors in mediating beta amyloid (Aβ)-induced inflammation. *J Neuroinflamm*. 2017;14(1):199. https://doi.org/10.1186/s12974-017-0972-9.
9 Chen Y, Song SH, Parhizkar S, et al. APOE3ch alters microglial response and suppresses Aβ-induced tau seeding and spread. *Cell*. 2023;187(2):428-445.e20. https://doi.org/10.1016/j.cell.2023.11.029.
10 Feng YS, Tan ZX, Wu LY, et al. The involvement of NLRP3 inflammasome in the treatment of Alzheimer's disease. *Ageing Res Rev*. 2020;64:101192. https://doi.org/10.1016/j.arr.2020.101192.
11 Heneka MT, Kummer MP, Stutz A, et al. NLRP3 is activated in Alzheimer´s disease and contributes to pathology in APP/PS1 mice. *Nature*. 2013;493(7434):674-678. https://doi.org/10.1038/nature11729.
12 Ising C, Venegas C, Zhang SS, et al. NLRP3 inflammasome activation drives tau pathology. *Nature*. 2019;575(7784):669-673. https://doi.org/10.1038/s41586-019-1769-z.
13 Yao J, Wang Z, Song WH, et al. Targeting NLRP3 inflammasome for neurodegenerative disorders. *Mol Psychiatry*. 2023;28(11):4512-4527. https://doi.org/10.1038/s41380-023-02239-0.
14 Bergsbaken T, Fink SL, Cookson BT. Pyroptosis: host cell death and inflammation. *Nat Rev Microbiol*. 2009;7(2):99-109. https://doi.org/10.1038/nrmicro2070.
15 Zhong Z, Liang S, Sanchez-Lopez E, et al. New mitochondrial DNA synthesis enables NLRP3 inflammasome activation. *Nature*. 2018;560(7717):198-203. https://doi.org/10.1038/s41586-018-0372-z.
16 Shimada K, Crother TR, Karlin J, et al. Oxidized mitochondrial DNA activates the NLRP3 inflammasome during apoptosis. *Immunity*. 2012;36(3):401-414. https://doi.org/10.1016/j.immuni.2012.01.009.
17 Wang YF, Shi PL, Chen Q, et al. Mitochondrial ROS promote macrophage pyroptosis by inducing GSDMD oxidation. *J Mol Cell Biol*. 2019;11(12):1069-1082. https://doi.org/10.1093/jmcb/mjz020.
18 Klemmensen MM, Borrowman SH, Pearce C, et al. Mitochondrial dysfunction in neurodegenerative disorders. *Neurotherapeutics*. 2023;21(1):e00292. https://doi.org/10.1016/j.neurot.2023.10.002.
19 Luo ZY, Dong JC, Wu JF. Impact of icariin and its derivatives on inflammatory diseases and relevant signaling pathways. *Int Immunopharmacol*. 2022;108:108861. https://doi.org/10.1016/j.intimp.2022.108861.
20 Wu Y, Wang XQ, Wu JY, et al. A tri-compound formula comprising ginsenoside Rg1, tetrandrine and icariin alleviates atopic dermatitis symptoms in a mouse model. *Phytomedicine*. 2025;141:156737. https://doi.org/10.1016/j.phymed.2025.156737.
21 Liu YQ, Li HL, Wang XW, et al. Anti-Alzheimers molecular mechanism of icariin: insights from gut microbiota, metabolomics, and network pharmacology. *J Transl Med*. 2023;21:277. https://doi.org/10.1186/s12967-023-04137-z.
22 Wang J, Liu YY, Wu YX, et al. Anti-inflammatory effects of icariin in the acute and chronic phases of the mouse pilocarpine model of epilepsy. *Eur J Pharmacol*. 2023;960:176141. https://doi.org/10.1016/j.ejphar.2023.176141.
23 Zhang TC, Lin YC, Sun NN, et al. Icariin, astragaloside a and puerarin mixture attenuates cognitive impairment in APP/PS1 mice *via* inhibition of ferroptosis-lipid peroxidation. *Neurochem Int*. 2024;175:105705. https://doi.org/10.1016/j.neuint.2024.105705.
24 Zhao H, Zhang SS, Gong Z, et al. Icariin mitigates depressive-like behavior in rats by regulating mitochondrial function. *J Ethnopharmacol*. 2025;350:120036. https://doi.org/10.1016/j.jep.2025.120036.
25 Min-Kaung-Wint-Mon, Kida H, Kanehisa I, et al. Adverse effects of $A\beta_{1-42}$ oligomers: impaired contextual memory and altered intrinsic properties of CA1 pyramidal neurons. *Biomolecules*. 2024;14(11):1425. https://doi.org/10.3390/biom14111425.
26 Li HL, Xiao Q, Zhu LM, et al. Targeting ceramide-induced microglial pyroptosis: icariin is a promising therapy for Alzheimer's disease. *J Pharm Anal*. 2025;15(4):101106. https://doi.org/10.1016/j.jpha.2024.101106.
27 Deacon RM. Assessing nest building in mice. *Nat Protoc*. 2006;1(3):1117-1119. https://doi.org/10.1038/nprot.2006.170.
28 Denninger JK, Smith BM, Kirby ED. Novel object recognition and object location behavioral testing in mice on a budget. *JoVE*. 2018(141):58593. https://doi.org/10.3791/58593.
29 Seibenhener ML, Wooten MC. Use of the open field maze to measure locomotor and anxiety-like behavior in mice. *J Visualized Exp*. 2015(96):52434. https://doi.org/10.3791/52434-v.
30 Kraeuter AK, Guest PC, Sarnyai Z. The Y-Maze for Assessment of Spatial Working and Reference Memory in Mice. In: Guest PC, ed. *Pre-Clinical Models*. Vol 1916. Methods in Molecular Biology. Springer New York; 2019:105-111. https://doi.org/10.1007/978-1-4939-8994-2_10.
31 Bespalov A, Steckler T. Pharmacology of anxiety or pharmacology of elevated plus maze? *Biol Psychiat*. 2021;89(12):e73. https://doi.org/10.1016/j.biopsych.2020.11.026.
32 Vorhees CV, Williams MT. Morris water maze: procedures for assessing spatial and related forms of learning and memory. *Nat Protoc*. 2006;1(2):848-858. https://doi.org/10.1038/nprot.2006.116.
33 Hickman S, Izzy S, Sen P, et al. Microglia in neurodegeneration. *Nat Neurosci*. 2018;21(10):1359-1369. https://doi.org/10.1038/s41593-018-0242-x.
34 Kovacs SB, Miao EA. Gasdermins: effectors of pyroptosis. *Trends Cell Biol*. 2017;27(9):673-684. https://doi.org/10.1016/j.tcb.2017.05.005.
35 Chen WF, Wu L, Du ZR, et al. Neuroprotective properties of icariin in MPTP-induced mouse model of Parkinson's disease: involvement of PI3K/Akt and MEK/ERK signaling pathways. *Phytomedicine*. 2017;25:93-99. https://doi.org/10.1016/j.phymed.2016.12.017.
36 Cai YW, Chai YH, Fu YX, et al. Salidroside ameliorates Alzheimer's disease by targeting NLRP3 inflammasome-mediated pyroptosis. *Front Aging Neurosci*. 2022;13:809433. https://doi.org/10.3389/fnagi.2021.809433.
37 Moonen S, Koper MJ, Van Schoor E, et al. Pyroptosis in Alzheimer's disease: cell type-specific activation in microglia, astrocytes and neurons. *Acta Neuropathol*. 2023;145(2):175-195. https://doi.org/10.1007/s00401-022-02528-y.
38 Fang EF, Hou Y, Palikaras K, et al. Mitophagy inhibits amyloid-β and tau pathology and reverses cognitive deficits in models of Alzheimer's disease. *Nat Neurosci*. 2019;22(3):401-412. https://doi.org/10.1038/s41593-018-0332-9.
39 Gu YY, Zhao XR, Zhang N, et al. Mitochondrial dysfunction as a therapeutic strategy for neurodegenerative diseases: current insights and future directions. *Ageing Res Rev*. 2024;102:102577. https://doi.org/10.1016/j.arr.2024.102577.
40 Kim J, Lee HJ, Park SK, et al. Donepezil regulates LPS and Aβ-stimulated neuroinflammation through MAPK/NLRP3 inflammasome/STAT3 signaling. *Int J Mol Sci*. 2021;22(19):10637. https://doi.org/10.3390/ijms221910637.
41 Zheng LY, Wu SC, Jin HC, et al. Molecular mechanisms and therapeutic potential of icariin in the treatment of Alzheimer's disease. *Phytomedicine*. 2023;116:154890. https://doi.org/10.1016/j.phymed.2023.154890.
42 Wang SG, Ma JR, Zeng YQ, et al. Icariin, an up-and-coming bioactive compound against neurological diseases: network pharmacology-based study and literature review. *Drug Des Devel Ther*. 2021;15:3619-3641. https://doi.org/10.2147/DDDT.S310686.
43 Wang YL, Shang C, Zhang Y, et al. Regulatory mechanism of icariin in cardiovascular and neurological diseases. *Biomed Pharmacother*. 2023;158:114156. https://doi.org/10.1016/j.biopha.2022.114156.
44 Xu WJ, Ding J, Kuang SD, et al. Icariin-Curcumol promotes docetaxel sensitivity in prostate cancer through modulation of the PI3K-Akt signaling pathway and the Warburg effect. *Cancer Cell Int*. 2023;23(1):190. https://doi.org/10.1186/s12935-023-03042-1.
45 El-Shitany NA, Eid BG. Icariin modulates carrageenan-induced acute inflammation through HO-1/Nrf2 and NF-κB signaling pathways. *Biomed Pharmacother*. 2019;120:109567. https://doi.org/10.1016/j.biopha.2019.109567.
46 Mangan MSJ, Olhava EJ, Roush WR, et al. Targeting the NLRP3 inflammasome in inflammatory diseases. *Nat Rev Drug Discov*. 2018;17(8):588-606. https://doi.org/10.1038/nrd.2018.97.